APPLIED SCIENCES AND ENGINEERING

Activation of Piezo1 promotes osteogenic differentiation of aortic valve interstitial cell through YAP-dependent glutaminolysis

Guoheng Zhong[1,2,3]†, **Shuwen Su**[1,2,3]†, **Juncong Li**[1,2,3], **Hengli Zhao**[1,2,3], **Dongtu Hu**[1,2,3], **Jun Chen**[1,2,3], **Shichao Li**[1,2,3], **Yingwen Lin**[1,2,3], **Liming Wen**[1,2,3], **Xiangjie Lin**[1,2,3], **Gaopeng Xian**[1,2,3], **Dingli Xu**[1,2,3]*, **Qingchun Zeng**[1,2,3]*

Hemodynamic overload and dysregulation of cellular metabolism are involved in development of calcific aortic valve disease (CAVD). However, how mechanical stress relates to metabolic changes in CAVD remains unclear. Here, we show that Piezo1, a mechanosensitive ion channel, regulated glutaminase 1 (GLS1)–mediated glutaminolysis to promote osteogenic differentiation of valve interstitial cells (VICs). In vivo, two models of aortic valve stenosis were constructed by ascending aortic constriction (AAC) and direct wire injury (DWI). Inhibition of Piezo1 and GLS1 in these models respectively mitigated aortic valve lesion. In vitro, Piezo1 activation induced by Yoda1 and oscillatory stress triggered osteogenic responses in VICs, which were prevented by Piezo1 inhibition or knockdown. Mechanistically, Piezo1 activation promoted calcium-dependent Yes-associated protein (YAP) activation. YAP modulated GLS1-mediated glutaminolysis, which enhanced osteogenic differentiation through histone acetylation of runt-related transcription factor 2 (RUNX2) promoters. Together, our work provided a cross-talk between mechanotransduction and metabolism in the context of CAVD.

INTRODUCTION

Calcific aortic valve disease (CAVD) is a common cardiovascular disease with high morbidity and mortality in developed countries (*1*). It is characterized by thickening and calcification of the aortic valve, which further progress into a series of atypical hemodynamic changes and, in due course, with severe aortic valve stenosis (*2*). However, there are no effective pharmacological interventions to terminate the progression of CAVD. Surgical and transcatheter aortic valve replacement (TAVR) remain the standard treatment for severe aortic stenosis patients (*3*).

Aortic valve interstitial cells (VICs), as the main cell population in aortic valves, play a key role in the development of CAVD. VICs stay quiescent in healthy aortic valve. In response to various pathological factors, such as proinflammatory cytokines and mechanical stress, the quiescent VICs can transform into myofibroblast- and osteoblast-like cells, which is recognized as the fundamental hallmark of the onset of CAVD. Mechanical stress is one of the major contributors to the onset and development of CAVD. Altered shear stress not only activates the endothelial cells but also recruits circulating monocytes to promote local valvular inflammation (*4*–*6*). Multiple previous studies have shown that mechanical cues such as matrix or substrate stiffness promoted myofibroblastic and osteogenic differentiation of VICs (*7*–*9*).

Piezo1, as a newly found mechanosensitive nonselective ion channel, identifies various mechanical stresses (e.g., shear stress, membrane stretch, matrix stiffness, compressive stress, and osmotic stress) and regulates physiological function of various tissue cells (*10*, *11*). It was reported that Piezo1 is associated with cardiovascular mechanobiology (*12*–*14*). Piezo1 activation by high shear stress enhanced the cellular expression of inflammatory cytokines in monocytes and increased monocyte adhesion to endothelial cells in aortic valve (*15*). Yoda1, a specific chemical agonist of Piezo1, keeps Piezo1 channel open by lowering the channel's mechanical threshold for activation (*16*, *17*). In addition to promoting monocyte recruitment and inflammation, Piezo1 activation may alter cellular metabolism. It was reported that Piezo1 participated in the remodeling of small arteries by stimulating activity of transglutaminases in smooth muscle cells (*18*) and promoted aerobic glycolysis in macrophages (*19*).

Recently, metabolism changes have drawn emerging attention and been considered as a responder for mechanical stimuli and a requirement for cell fate transitions. Increasing evidences suggest that a central connection of mechanotransduction with cellular metabolism through Yes-associated protein (YAP) pathway (*20*–*22*), which was mechanoactivated by mechanical stimuli, functions as a transcription coactivator to regulate target gene transcription (*23*). YAP signaling has previously been demonstrated as a mechanosensitive controller of VIC differentiation in response to substrate stiffness (*24*, *25*). Moreover, it was reported that metabolic reprogramming provides substrates or cofactors of chromatin-modifying enzymes for epigenetic modifications, and eventually controls cell fate and function. One of the most representative metabolic processes is glutaminolysis, which begins with the lysis of glutamine to glutamate, and then further yields many metabolites such as acetyl–coenzyme A (CoA) to regulate histone acetylation. Glutaminase 1 (GLS1), the key enzyme in glutaminolysis, has recently been shown to promote the inflammatory response and chondrocytic genes expression in chondrocyte, as well as myofibroblast formation and persistence in heart failure (*26*, *27*). Glutamine

---

[1] State Key Laboratory of Organ Failure Research, Department of Cardiology, Nanfang Hospital, Southern Medical University, Guangzhou 510515, China. [2] Guangdong Provincial Key Laboratory of Shock and Microcirculation, Southern Medical University, Guangzhou 510515, China. [3] Bioland Laboratory (Guangzhou Regenerative Medicine and Health Guangdong Laboratory), Guangzhou, China.
*Corresponding author. Email: dinglixu@smu.edu.cn (D.X.); qingchunzeng@smu.edu.cn. (Q.Z.)
†These authors contributed equally to this work.

metabolism has been linked to pathological cell proliferation in cancer and cellular senescence, which may be relevant to CAVD, an age-associated disorder (*28*). However, the cross-talk of Piezo1 activation and glutamine metabolism remains poorly understood and how the metabolic changes regulate VIC differentiation needs further investigation.

Consequently, in this study, we investigated whether Piezo1 activation alters glutamine metabolism to regulate osteogenic differentiation. Specifically, we found that Piezo1 was highly expressed in human calcific aortic valves. We also demonstrate that in response to ascending aortic constriction (AAC) and direct wire injury (DWI)–induced hemodynamic overload, mice aortic valves showed increased expression of Piezo1 and calcification, while inhibition of Piezo1 by Dooku1 attenuated these changes. Piezo1 activation by Yoda1 triggers GLS1-mediated glutamine metabolic reprogramming by YAP mechanotransduction and was associated with CAVD progression in vitro. Further study showed that glutamine metabolism promotes histone acetylation. Inhibition of GLS1 ameliorated osteogenic differentiation in vitro and in vivo. Therefore, this study provides a cross-talk between Piezo1 activation and glutamine metabolism in the development of CAVD.

RESULTS

Patients with CAVD have increased Piezo1 expression in aortic valve tissue and elevated glutaminolysis in plasma

To determine the association between expression of Piezo1 and metabolic changes in CAVD, we first collected human aortic valves in patients with or without CAVD (patient information shown in table S1). We examined the expression of Piezo1 in calcific aortic valves and normal aortic valves. Using quantitative polymerase chain reaction (qPCR) analysis, we found that *Piezo1*, not *Piezo2*, was increased in calcific aortic valves (Fig. 1, A and B). Similarly, immunoblots showed that the protein expression was highly expressed in calcific aortic valves (Fig. 1, C and D, and fig. S1A). Masson's trichrome staining and alizarin red staining showed severe fibrocalcific remodel in aortic valves from CAVD patients (Fig. 1E and fig. S1B). We then used immunohistochemical staining to test the distribution of Piezo1 in the three-layer structure of human aortic valve leaflets, including the spongiosa layer (Spg), fibrous layer (Fbs), and ventricular layer (Vet). Normal rabbit immunoglobulin G (IgG) as the negative control antibody revealed no staining over the background in aortic valves from either normal or CAVD groups (fig. S1C). We found that compared with normal aortic valves, Piezo1 expression was elevated in all three-layer structures in calcific aortic valves, especially primarily distributed in the Spg layer, with Fbs and Vet layers following. Aortic valves from both normal and CAVD groups showed relatively high expression in the endothelium of the aortic side, which may be relevant to the fluid shear stress (Fig. 1F). Immunofluorescence further revealed that the expression of Piezo1 was up-regulated and colocalized with osteogenic marker runt-related transcription factor 2 (RUNX2) in aortic valves from CAVD group (Fig. 1G). Piezo1 was also colocalized with CD31, a marker of endothelial cells (Fig. 1H).

To test the possible metabolic changes between patients with CAVD and the control group, we collected peripheral venous plasma from CAVD and age-matched non-CAVD patients (table S2) and measured candidate metabolites that reflect the activity of glutaminolysis, glycolysis, anaplerosis, and the tricarboxylic acid (TCA) cycle by liquid chromatography–tandem mass spectrometry (LC-MS/MS) in peripheral venous plasma. We observed markedly decreased glutamine level and increased glutamate level (fig. S2, A and B), while lactate, aspartate, and pyruvate levels were not significantly changed in the CAVD group (fig. S2, C to E). Together, CAVD was associated with high expression of Piezo1 in aortic valve tissue and increased glutaminolysis in plasma.

Inhibition of Piezo1 ameliorates AAC- and DWI-induced aortic valve calcification in mice

Since Piezo1 serves as an ion channel to sense fluid stress and regulate cell function, we investigated whether high shear stress in aortic root could activate the expression of Piezo1 and induce valve calcification, and inhibition of Piezo1 could prevent the aortic valve calcification. For this purpose, we induced pressure overload in mice valve leaflets by AAC (fig. S3, A and B). At the same time, another CAVD model was constructed by direct wire injury (DWI) to the aortic valve (fig. S5, A and B). Then, we administered vehicle or the Piezo1 inhibitor Dooku1 (10 mg/kg) via intraperitoneal injection every other day. After 8 weeks, echocardiographic assessment of mice in both AAC and DWI groups showed a notable increase in aortic valve (AV) peak velocity mean gradient compared with those in the sham group, while inhibition of Piezo1 restored these changes (Fig. 2, A and B, and figs. S3C and S4C). Additional echocardiographic parameters related to cardiac function can be found in figs. S3 (D to H) and S5 (D to H). Both ejection fraction (EF) and fractional shortening (FS) declined markedly in AAC + Vehicle and DWI + Vehicle groups, accompanied by increased left ventricular (LV) mass, diastolic LV inner diameter (LVIDd), and systolic LV inner diameter (LVIDs) compared with the sham group, while Dooku1 treatment in both models partially preserved the cardiac function in two models. We further found that aortic valves in both AAC and DWI groups showed much more severe thickness, calcification, and fibrosis than those of sham, whereas Dooku1 intervention alleviated these changes, as evidenced by hematoxylin and eosin (H&E) staining (Fig. 2, C and D), von Kossa staining (Fig. 2, E and F), alizarin red staining (figs. S4A and S6A), and Masson's staining (figs. S4B and S6B). We also observed that Piezo1 expression was markedly increased in the aortic valve in AAC and DWI mice, and Dooku1 partially decreased Piezo1 expression (Fig. 2, G to J). Besides, the osteogenic differentiation marker Runx2 was significantly up-regulated in AAC and DWI mice, while inhibition of Piezo1 reduced osteogenic differentiation (Fig. 2, K and L). In addition, we observed that both AAC- and DWI-operated mice showed increased macrophage infiltration, as indicated by CD68, the macrophage marker, whereas a reduced number of macrophages were observed in the Dooku1-treated mice (figs. S4C and S6C). We also found that Piezo1 expression was up-regulated in endothelial cells (CD31 positive) of both two models, while Dooku1 treatment reduced Piezo1 expression in $CD31^+$ cells (fig. S7, A and B). These results suggested that high mechanical stress in aortic valve by AAC and DWI models activated Piezo1 expression and induced aortic valve calcification, while inhibition of Piezo1 by Dooku1 partially prevented these changes.

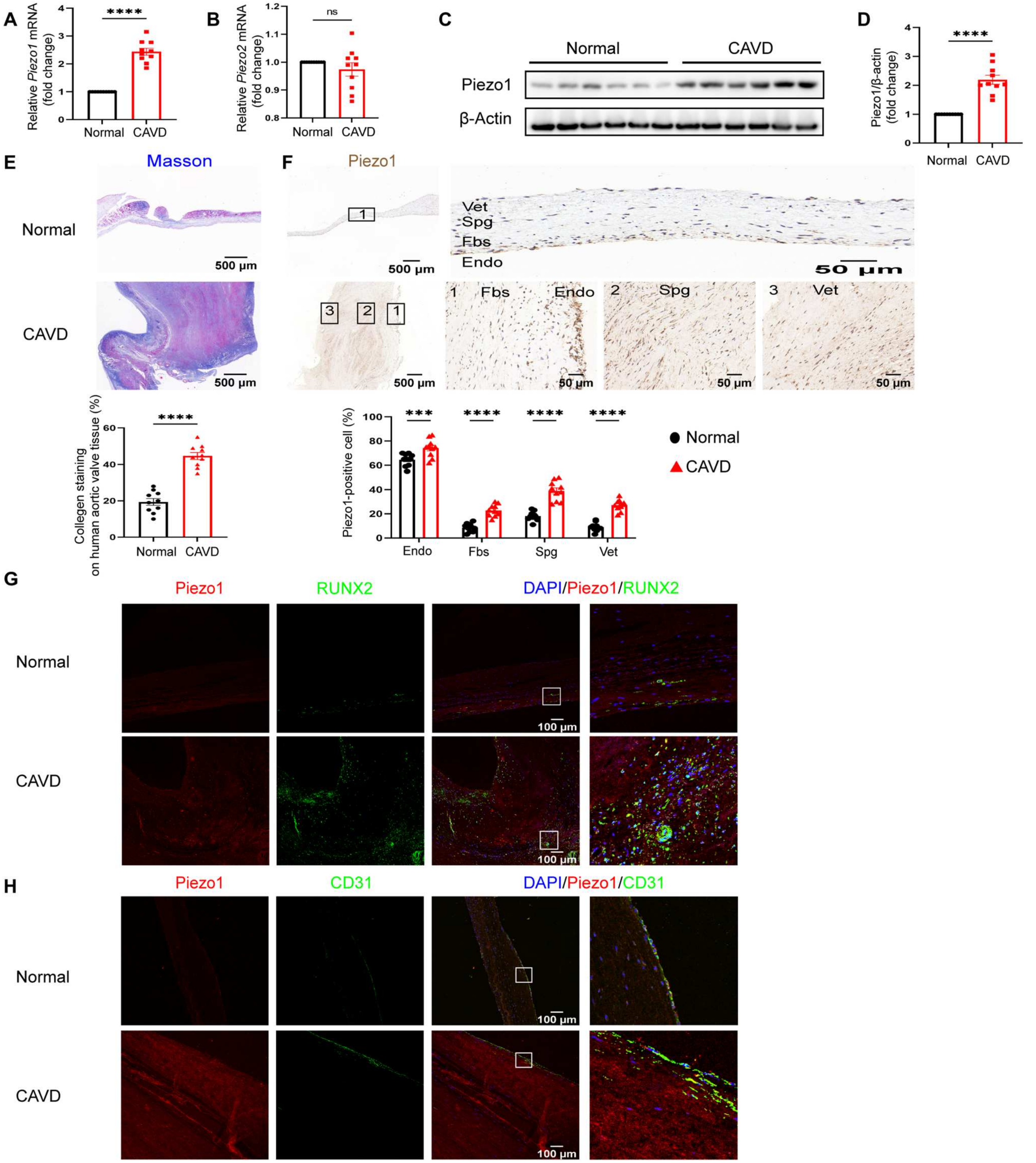

Fig. 1. Increased expression of Piezo1 in CAVD. (**A** and **B**) mRNA level of *Piezo1* and *Piezo2* in human aortic valve from CAVD and normal groups ($n = 10$). (**C** and **D**) Representative immunoblots and densitometric data showed protein Piezo1 level in the CAVD group and non-CAVD ($n = 10$, 6 versus 6 were shown in this figure, another 4 versus 4 were shown in fig. S1A). (**E**) Masson's trichrome staining of collagen in human aortic valve; scale bar, 100 μm; $n = 10$. (**F**) Immunohistochemical staining showed Piezo1 protein localization in normal and CAVD aortic valve tissue in full size (left; scale bar, 500 μm) and in enlarged images (right; scale bar, 50 μm); $n = 10$. (**G**) Representative immunofluorescence images showed that Piezo1 protein colocalized with RUNX2 in human aortic valve tissue from normal and CAVD groups. Scale bar, 100 μm; $n = 10$. (**H**) Representative images of immunofluorescence staining for CD31 (green) and Piezo1 (red) in aortic valve. Scale bar, 100 μm; $n = 10$. Data are means ± SEM (Student's *t* test). $^{***}P < 0.001$; $^{****}P < 0.0001$; ns, $P > 0.05$.

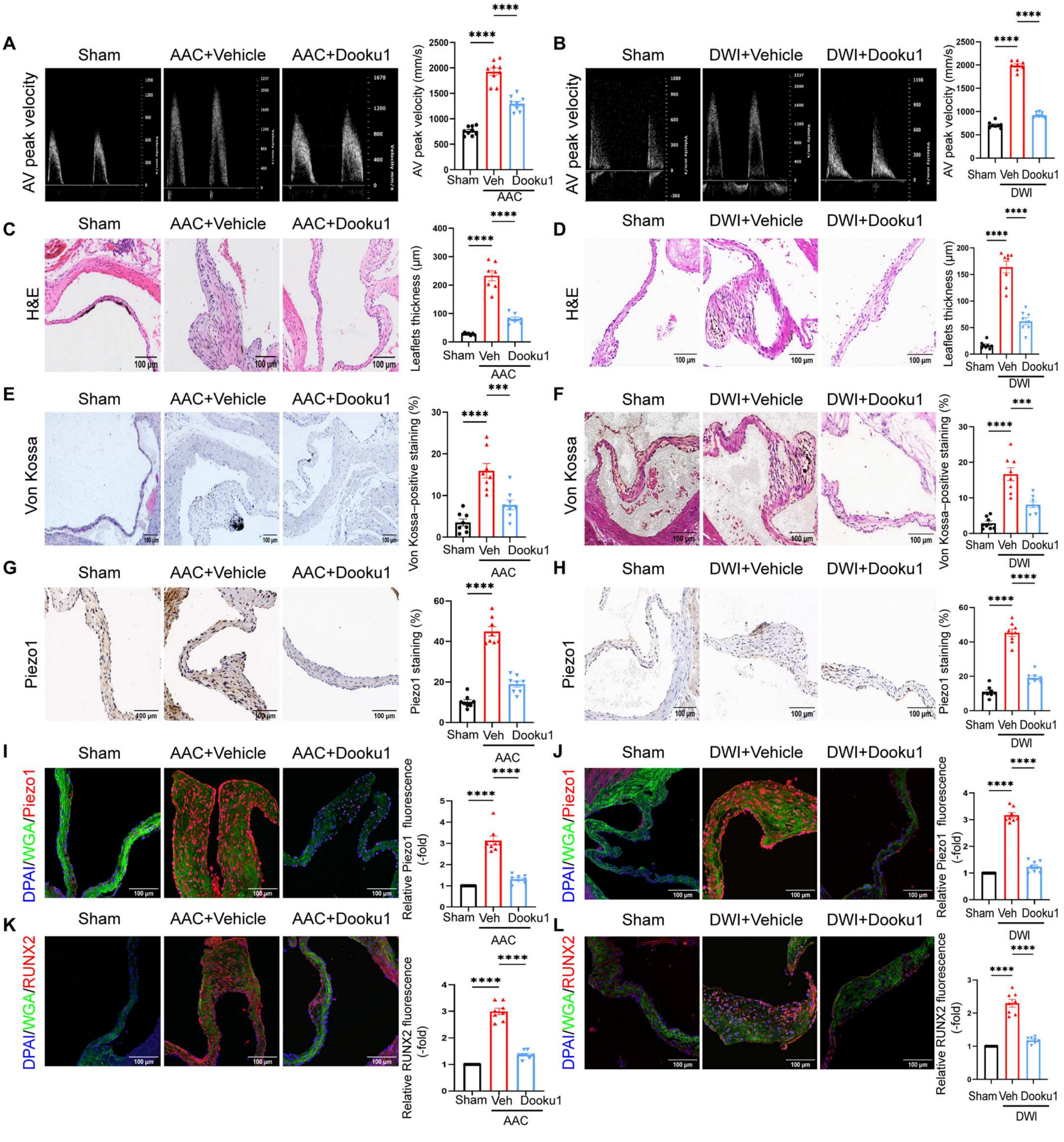

Fig. 2. Inhibition of Piezo1 prevents AAC- and DWI-induced aortic valve calcification. (**A** and **B**) Aortic valve (AV) peak velocity of C57BL/6J mice treated with Sham, AAC + Vehicle, and AAC + Dooku1 (*n* = 8 per group), as well as C57BL/6J mice treated with Sham, DWI + Vehicle, and DWI + Dooku1 (*n* = 8 per group). (**C** and **D**) H&E staining of aortic valve leaflets from C57BL/6J mice treated with Sham, AAC + Vehicle, and AAC + Dooku1 (*n* = 8 per group), as well as C57BL/6J mice treated with Sham, DWI + Vehicle, and DWI + Dooku1 (*n* = 8 per group); scale bar, 100 μm. (**E** and **F**) Representative image of von Kossa staining of mice aortic valve leaflets in AAC-treated mice (*n* = 8 per group) and DWI-treated mice (*n* = 8 per group); scale bar, 100 μm. (**G** and **H**) Representative images of immunohistochemical Piezo1 staining in AAC-treated mice (*n* = 8 per group) and DWI-treated mice (*n* = 8 per group); scale bar, 100 μm. (**I** to **L**) Representative images of Piezo1 (I) and (J) and RUNX2 (K) and (L) immunofluorescence in AAC-treated mice (*n* = 8 per group) and DWI-treated mice (*n* = 8 per group); scale bar, 100 μm. Data are means ± SEM. ***$P < 0.001$; ****$P < 0.0001$; ns, $P > 0.05$.

Activation of Piezo1 promotes osteogenic phenotypes in human aortic VICs

To further examine the association between Piezo1 and aortic valve calcification in vitro, we used the Piezo1-specific agonist Yoda1 to treat human aortic VICs. Primary aortic VICs were isolated from human aortic valves and cultured until passage 7. Immunofluorescence staining confirmed that the isolated VICs were positive for vimentin but negative for CD31 (fig. S8). We first determined the effect of various concentrations of Yoda1 (0, 2.5, 5, and 10 μM) on the myofibroblastic and osteogenic responses in human VICs from normal and CAVD aortic valves. As shown in Fig. 3A and fig. S9A, stimulation with Yoda1 resulted in a dose-dependent increase of osteogenic markers alkaline phosphatase (ALP), RUNX2, and bone morphogenetic protein 2 (BMP2) and the myofibroblast marker α-smooth muscle actin (α-SMA) (Fig. 3A and figs. S9A and S10A). In addition, the myofibroblastic and osteogenic response was greater in VICs of CAVD when the concentration of Yoda1 reached 5 μM, compared with the normal group. To further validate the profibrotic-osteogenic effect of Piezo1 in VICs, we used the Piezo1 inhibitor Dooku1 to pretreat VICs. As expected, inhibition of Piezo1 by Dooku1 dose dependently reduced myofibro-osteogenic marker expression in response to Yoda1, with a greater reduction in cells from CAVD valves (Fig. 3B and figs. S9B and S10B). Moreover, we stimulated VICs from normal aortic valves with Yoda1 in the presence and absence of Dooku1 to determine the effect of Piezo1 on in vitro osteogenic activity. We observed that Yoda1 promoted the accumulation of calcium deposits and the activity of ALP in VIC osteogenic medium culture, as evidenced by alizarin red and ALP staining, while inhibition of Piezo1 reduced osteogenic differentiation in VICs (Fig. 3, C and D). To determine whether Piezo1 modulates the osteogenic responses, we performed Piezo1 knockdown in VICs from normal aortic valves. Consistent with pharmacologic inhibition of Piezo1, Piezo1 knockdown with small interfering RNA (siRNA) markedly reduced the protein level of ALP, RUNX2, and BMP2 in VICs, as evidenced by immunoblots and immunofluorescence staining of RUNX2 (Fig. 3, E and F). Similarly, Piezo1 knockdown reduced α-SMA expression (fig. S10C). Furthermore, in response to Yoda1, VICs in the si-Piezo1 group showed less calcium deposits and activity of ALP than the scrambled siRNA group (Fig. 3, G and H). These results show that activation of Piezo1 by Yoda1 induced osteogenic differentiation in VICs, which could be improved by inhibition or knockdown of Piezo1.

Piezo1 activates YAP in human VICs

YAP, as a mechanosensitive transcriptional activator, plays a critical role in tissue homeostasis and cell differentiation, and its signaling pathway can be regulated by mechanical stress (*23*). Since mechanical stress stimulates the activity of Piezo1, we hypothesized that Piezo1 activates YAP to promote osteogenic differentiation in aortic valve. We first tested the expression of YAP and its phosphorylation under Yoda1 stimulation and found that YAP expression was increased in a dose-dependent manner, while its phosphorylation was significantly decreased. Furthermore, VICs from CAVD aortic valves showed greater YAP expression than that of the normal group (Fig. 4A). To further investigate the function of YAP in Piezo1-induced aortic valve fibrosis and calcification, we pretreated normal VICs with a specific YAP inhibitor, verteporfin, and then exposed them to Yoda1. Western blots were conducted to detect the protein expression of ALP, RUNX2, BMP2, and α-SMA. As expected, inhibition of YAP in VICs suppressed osteogenic responses in Yoda1-induced VICs (Fig. 4B and fig. S11A). Further study found that inhibition of YAP attenuated the production of calcium deposition and the activity of ALP in normal VICs (Fig. 4, C and D). We further confirmed the role of YAP in the modulation of VIC osteogenic differentiation by transfecting with YAP siRNA or scramble RNA in VICs from normal aortic valves. Consistently, the expression of ALP, RUNX2, BMP2, and α-SMA was markedly lower in VICs with si-YAP compared with the scrambled siRNA group (Fig. 4, E and F), which coincided with a decrease in calcium deposition and ALP activity (Fig. 4, G and H). These results indicated that YAP was involved in Piezo1-mediated osteogenic differentiation.

Piezo1 drives YAP activation through intracellular Ca^{2+} accumulation

As a calcium-permeable ion channel, Piezo1 regulates Ca^{2+} homeostasis to control various signal activation. Moreover, calcium functions as a second messenger, which participates in action potential, contraction, transcription, and cell death. We hypothesized that Ca^{2+} is required for Piezo1-YAP mechanoactivation. We first detected the intracellular Ca^{2+} concentration in VICs using Fluo-4 AM. We found that Yoda1 significantly increased concentrations of cytosolic Ca^{2+}, whereas Piezo1 knockdown reduced the Ca^{2+} influx (Fig. 5A). Furthermore, we further performed immunofluorescence to assay YAP subcellular localization. We noticed that Yoda1 triggered YAP nucleus translocation, whereas Piezo1 knockdown arrested YAP in cytoplasm (Fig. 5B). The nucleocytoplasmic separation analysis consistently confirmed the Piezo1 regulation of YAP nucleus translocation (Fig. 5C). To investigate the role of Ca^{2+} influx in Piezo1-YAP mechanotransduction, we then treated VICs with or without 1,2-bis(2-aminophenoxy)ethane-*N*,*N*,*N*′,*N*′-tetraacetic acid (BAPTA)–AM following Yoda1 stimulation. BAPTA-AM is an intracellular Ca^{2+} chelator that acts as a Ca^{2+} sponge to reduce intracellular Ca^{2+} concentration. We observed that BAPTA-AM intervention abolished the intracellular Ca^{2+} accumulation induced by Yoda1 (Fig. 5D). Moreover, as shown in immunofluorescence, BAPTA-AM inhibited Yoda1-induced YAP nucleus translocation (Fig. 5E). Moreover, nucleocytoplasmic separation analysis showed that Yoda1-treated VICs displayed increased YAP expression in the nucleus, while BAPTA-AM treatment made YAP largely localized in the cytoplasm (Fig. 5F). These findings indicated that intracellular Ca^{2+} accumulation is responsible for Piezo1-induced YAP nucleus translocation.

Piezo1 modulates GLS1-mediated glutamine metabolism remodeling through YAP

It was reported that glutaminolysis, initiated by GLS1-mediated lysis of glutamine into glutamate, was related to mechanotransduction in tumor and pulmonary hypertension. To determine whether mechanical cues by Piezo1 modulate glutamine metabolism of VICs, we tested the *GLS1* mRNA and GLS1 protein expression in VICs from both normal and CAVD aortic valves with Yoda1 treatment compared with the control group (Fig. 6, A and B). As expected, both mRNA and protein expression of GLS1 were elevated under Yoda1 treatment, with greater increase in VICs of CAVD than that of the normal group. We further measured intracellular metabolites glutamine and glutamate. Yoda1 decreased intracellular

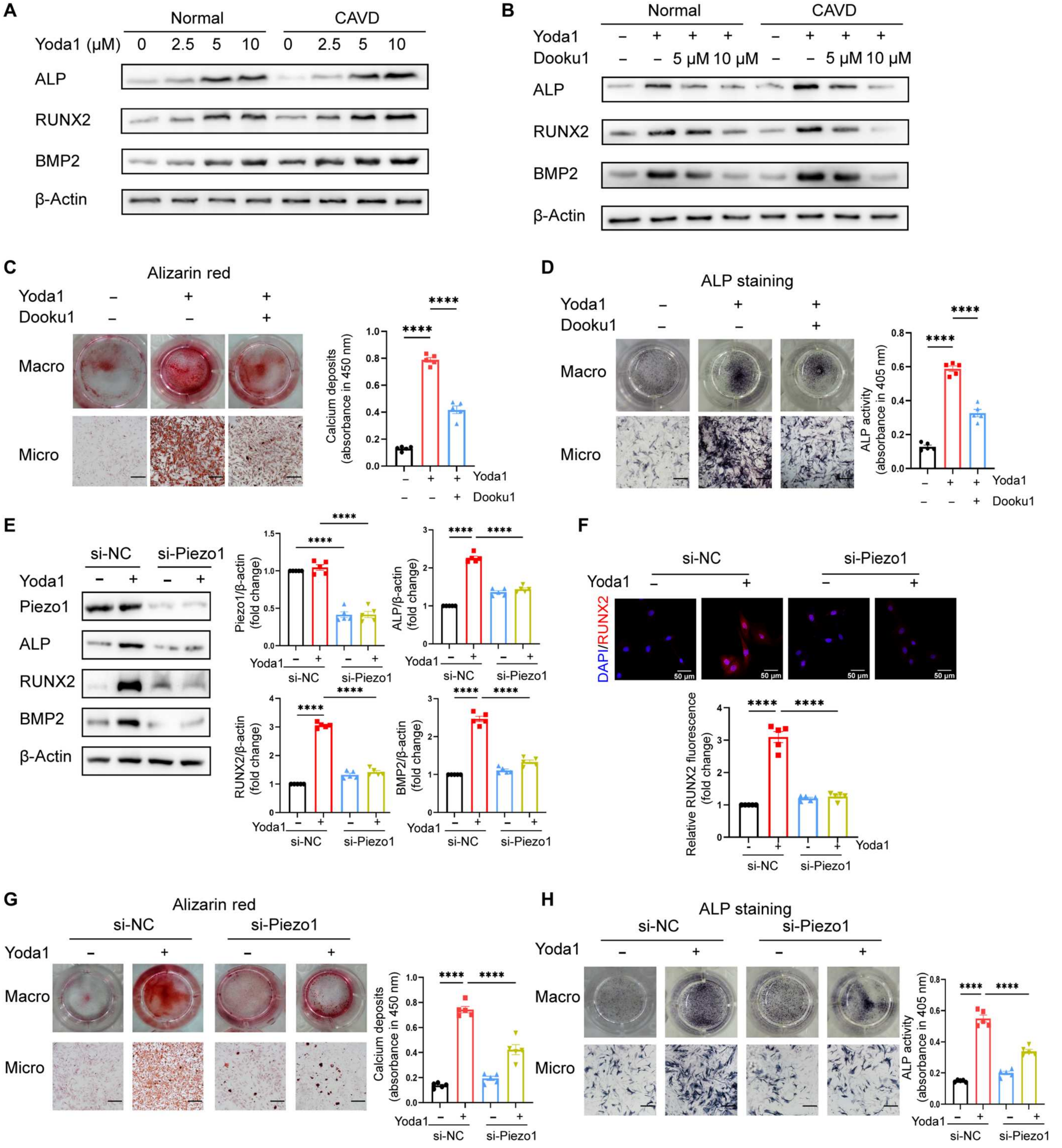

Fig. 3. Activation of Piezo1 by Yoda1 induced osteogenic differentiation of VICs. (**A**) Human aortic VICs from normal and CAVD aortic valves were treated with Yoda1 (0, 2.5, 5, and 10 μM) for 24 hours. Data showed ALP, RUNX2, and BMP2 protein levels; $n = 5$. (**B**) VICs from normal and CAVD aortic valves were pretreated with the Piezo1 inhibitor Dooku1. Representative immunoblots and densitometric data showed the protein level of ALP, RUNX2, and BMP2; $n = 5$. (**C**) Alizarin red staining of mineralization nodules showed that Dooku1 treatment significantly reduced Yoda1-induced mineralization nodule formation of normal VICs; $n = 5$; scale bar, 500 μm. (**D**) ALP staining showed that Dooku1 treatment significantly reduced Yoda1-induced ALP activity of VICs; $n = 5$; scale bar, 500 μm. (**E**) Representative immunoblots and densitometric data showed that knockdown of Piezo1 in normal VICs reduced Yoda1-induced osteogenic responses; $n = 5$. (**F**) Immunofluorescence staining of RUNX2 in VICs; $n = 5$; scale bar, 50 μm. (**G**) Alizarin red staining of mineralization nodules showed that knockdown of Piezo1 significantly reduced Yoda1-induced mineralization nodule formation of VICs; $n = 5$; scale bar, 500 μm. (**H**) ALP staining showed that knockdown of Piezo1 significantly reduced Yoda1-induced ALP activity of VICs; $n = 5$; scale bar, 500 μm. Data are means ± SEM. ****$P < 0.0001$; ns, $P > 0.05$.

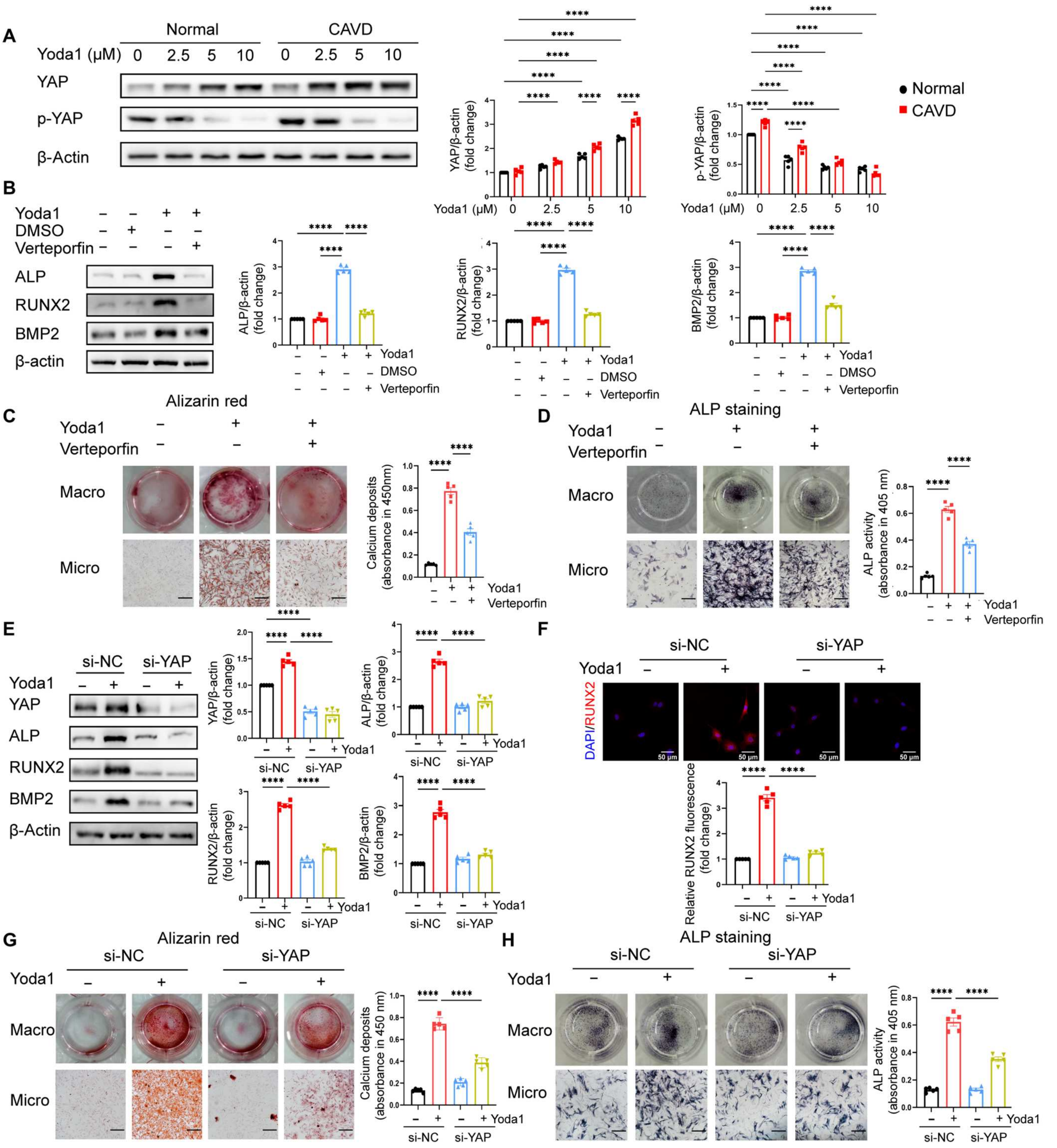

Fig. 4. Piezo1 activated YAP to control osteogenic differentiation of VICs. (**A**) Representative immunoblots and densitometric data showed YAP and its phosphorylation expression in VICs from normal and CAVD aortic valves under Yoda1 stimulation; *n* = 5. (**B**) Representative immunoblots and densitometric data showed that verteporfin markedly reduced Yoda1-induced osteogenic responses; *n* = 5. (**C**) Alizarin red staining of mineralization nodules showed that verteporfin treatment significantly reduced Yoda1-induced mineralization nodule formation of VICs; *n* = 5; scale bar, 500 μm. (**D**) ALP staining showed that verteporfin treatment significantly reduced Yoda1-induced ALP activity of VICs; *n* = 5; scale bar, 500 μm. (**E**) Representative immunoblots and densitometric data showed that knockdown of YAP reduced Yoda1-induced osteogenic responses in normal VICs; *n* = 5. (**F**) Immunofluorescence staining of RUNX2 in VICs; *n* = 5; scale bar, 50 μm. (**G**) Alizarin red staining of mineralization nodules showed that knockdown of YAP significantly reduced Yoda1-induced mineralization nodule formation of VICs; *n* = 5; scale bar, 500 μm. (**H**) ALP staining showed that knockdown of YAP significantly reduced Yoda1-induced ALP activity of VICs; *n* = 5; scale bar, 500 μm. Data are means ± SEM. ****$P < 0.0001$; ns, $P > 0.05$.

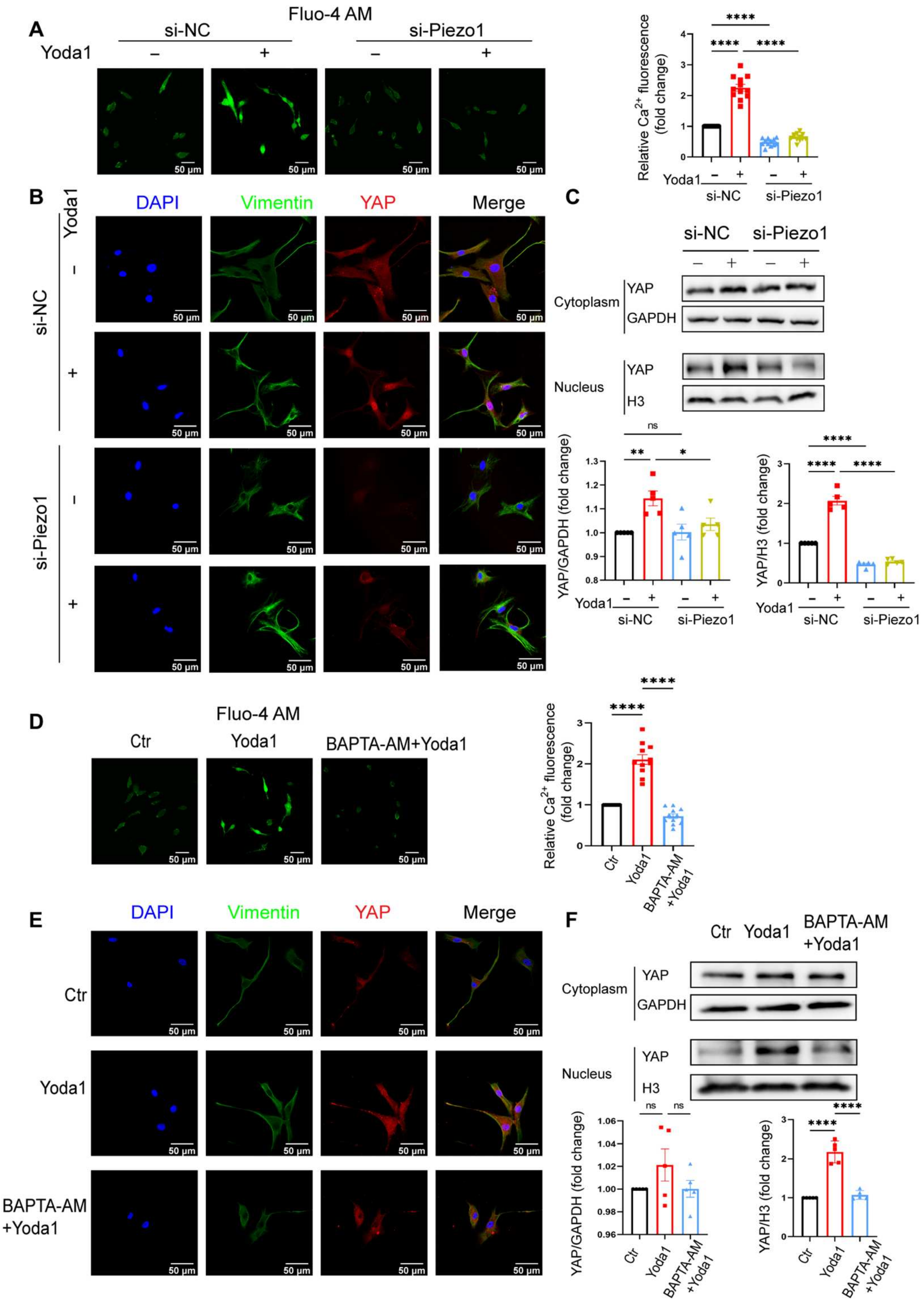

Fig. 5. Ca^{2+} influx is responsible for Piezo1-YAP mechanotransduction. (**A**) Representative fluorescence imaging of intracellular Ca^{2+} in VICs using Fluo-4 AM; $n = 5$; scale bar, 50 μm. (**B**) Immunofluorescence showed that Piezo1 knockdown inhibited YAP nucleus translocation; $n = 5$; scale bar, 50 μm. (**C**) Representative immunoblots and densitometric data showed that Piezo1 knockdown aborted YAP nucleus translocation induced by Yoda1; $n = 5$. (**D**) Representative fluorescence imaging of intracellular Ca^{2+} in VICs; $n = 12$; scale bar, 50 μm. (**E**) Immunofluorescence showed that Yoda1 promoted YAP nucleus translocation, which was blocked by BAPTA-AM; $n = 12$; scale bar, 50 μm. (**F**) Representative immunoblots and densitometric data showed that YAP was mainly localized in the nuclear by Yoda1 treatment but was largely localized in the cytoplasm by BAPTA-AM treatment; $n = 5$. Data are means ± SEM. $*P < 0.05$; $**P < 0.01$; $****P < 0.0001$; ns, $P > 0.05$.

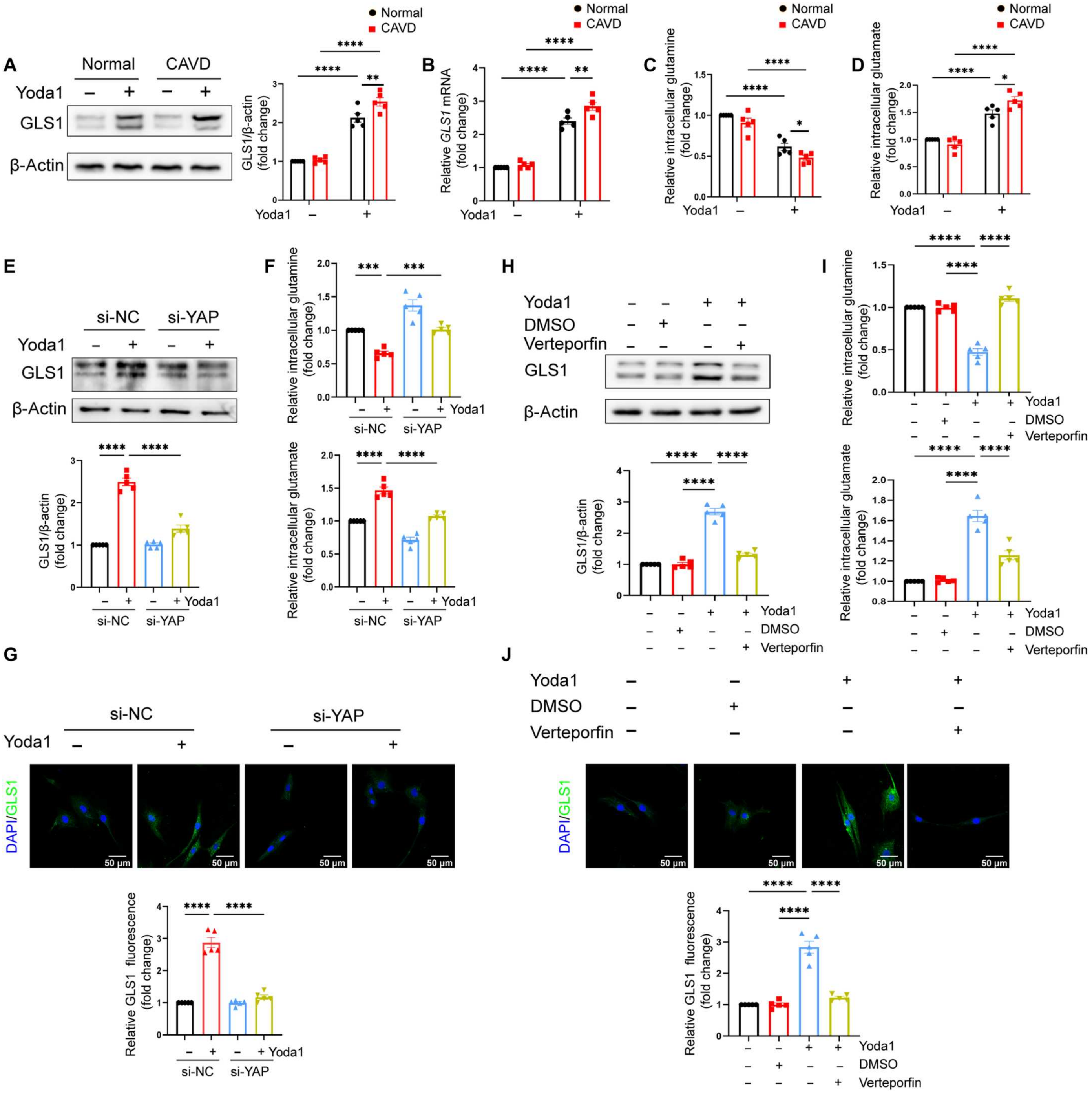

Fig. 6. Piezo1 modulates GLS1-mediated glutaminolysis through YAP. (**A**) Representative immunoblots and densitometric data showed that VICs from the CAVD group had greater GLS1 expression after Yoda1 stimulation. (**B**) Representative qPCR data showed mRNA level of *GLS1* in VICs; *n* = 5. (**C**) Intracellular metabolite glutamine in control and Yoda1-treated VICs from normal and CAVD groups; *n* = 5. (**D**) Intracellular metabolite glutamate in control and Yoda1-treated VICs from normal and CAVD groups; *n* = 5. (**E**) Representative immunoblots and densitometric data showed that, under Yoda1 treatment, normal VICs transfected with si-YAP showed reduced expression of GLS1 compared with scrambled siRNA–transfected normal VICs; *n* = 5. (**F**) Intracellular metabolites glutamine and glutamate in si-YAP and scrambled siRNA–transfected normal VICs with or without Yoda1 treatment; *n* = 5. (**G**) Representative immunofluorescence staining of GLS1; scale bar, 50 μm. (**H**) Representative immunoblots and densitometric data showed that YAP inhibitor verteporfin markedly reduced Yoda1-induced GLS1 expression; *n* = 5. (**I**) Intracellular metabolites glutamine and glutamate in VICs with Yoda1 and verteporfin treatment; *n* = 5. (**J**) Representative immunofluorescence staining of GLS1; scale bar, 50 μm. Data are means ± SEM. *$P < 0.05$; **$P < 0.01$; ***$P < 0.001$; ****$P < 0.0001$; ns, $P > 0.05$.

glutamine accompanied by an increase of glutamate, with greater effect of glutaminolysis in VICs of CAVD (Fig. 6, C and D). Since we previously found that YAP acts as a downstream mechanosensors of Piezo1 in VICs, we investigated whether YAP is crucial in modulating the mechanotransduction of Piezo1 on glutamine metabolic reprogramming. In VICs treated with Yoda1, knockdown of YAP with siRNA reduced GLS1 expression compared with the scrambled siRNA group, as evidenced by Western blots and immunofluorescence staining (Fig. 6, E and G). Knockdown of YAP also blunted the effects of Yoda1 on intracellular glutamine and glutamate. Accordingly, the effect of Yoda1 on intracellular glutamine and glutamate was also blunted by knockdown of YAP (Fig. 6F). Similarly, inhibition of YAP with verteporfin suppressed Yoda1-induced GLS1 expression and glutaminolysis (Fig. 6, H to J).

Glutamine metabolism remodeling regulates osteogenic differentiation of VICs through histone acetylation

To determine the role of GLS1 in osteogenic differentiation of VICs induced by Piezo1 activation, we used the GLS1-specific inhibitor bis-2-(5-phenylacetamido-1,3,4-thiadiazol-2-yl) ethyl sulfide (BPTES) in cultures of human VICs from normal aortic valves. We found that BPTES reduced the protein expression of ALP, RUNX2, BMP2, and α-SMA in Yoda1-induced VICs (Fig. 7A and fig. S12A). Moreover, the content of calcification nodules and ALP activity were also reduced in VICs treated with BPTES (Fig. 7, B and C). We further asked about the mechanism of how glutaminolysis enhances osteogenic differentiation of VICs. It was reported that GLS1 mediated the lysis of glutamine to glutamate, and the latter will then enter the citric acid cycle (TCA), which yields many intermediate metabolites such as acetyl-CoA. Acetyl-CoA is the acetyl carrier for histone acetylation, which links metabolism and epigenetics (*29*). We hypothesized that glutaminolysis might promote the myofibroblastic and osteogenic differentiation of VICs via an increase in acetyl-CoA–associated histone acetylation. Thus, we detected the acetyl-CoA concentration in Yoda1-induced VICs treated with or without BPTES and checked the acetylation status of histone 3 at lysine-27. The Yoda1-induced VICs showed increased production of acetyl-CoA and elevated histone acetylation, while BPTES reduced the effects (Fig. 7, D and E). Chromatin immunoprecipitation (ChIP)–PCR analysis showed that H3K27Ac enrichment in the RUNX2 gene promoter was notably increased by Yoda1, which was diminished by BPTES (Fig. 7F). Next, we directly added acetate to BPTES-treated cells, which can be converted into acetyl-CoA by acetyl-CoA synthesis, and found that acetate addition restored H3K27Ac levels (Fig. 7G).

Similarly, by silencing GLS1 in VICs of normal valves, osteogenic markers ALP, RUNX2, and BMP2 and myofibroblast marker α-SMA were markedly reduced (Fig. 7, H and I, and fig. S12B). GLS1 knockdown also reduced acetyl-CoA concentration (fig. S13A), as well as the level of H3K27Ac and its enrichment in the RUNX2 gene promoter (Fig. 7, J and K). Moreover, alizarin red staining and ALP staining indicated that GLS1 knockdown inhibited osteogenic differentiation of VICs (Fig. 7, L and M). Together, these results revealed that in VICs, H3K27 acetylation and osteogenic gene expression are dependent on GLS1-mediated glutamine metabolism.

Piezo1 mediates oscillatory stress–induced osteogenic responses through Piezo1-YAP-GLS1 axis in VICs

Because Piezo1 serves as an ion channel to sense fluid stress, Piezo1 activation by fluid stress may promote osteogenic responses in VICs. To investigate the role of fluid stress in myofibroblast and osteogenic responses in VICs, and the possible mechanism linking the Piezo1-YAP-GLS1 axis, we examined the responses of VICs to three different fluid conditions [static (ST), laminar stress (LS), and oscillatory stress (OS)]. As shown in fig. S14 (A and C), it is OS, not LS, that markedly increased expression of Piezo1 in VICs. We also found that YAP and GLS1 expression were decreased by LS but increased by OS. Moreover, OS promoted profibrotic and osteogenic responses in VICs, as evidenced by elevated expression of ALP, RUNX2, BMP2, and α-SMA (fig. S14B). We then assessed cellular Ca^{2+} in VICs after exposure to three different fluid conditions and found that OS had greater effect on the increased intracellular concentration of Ca^{2+} compared to LS (fig. S14D). To further confirm that Piezo1 was involved in OS-induced myofibroblastic and osteogenic differentiation of VICs, we performed Piezo1 knockdown in VICs and then exposed VICs to ST or OS. Piezo1 knockdown notably reduced the flow-mediated regulation of YAP and GLS1, as well as the myofibroblast marker and osteogenic markers (fig. S14, D and E). Together, these data indicated that Piezo1 is necessary for OS-induced VIC myofibroblastic and osteogenic differentiation.

Inhibition of GLS1 decreases glutaminolysis and consequent aortic valve calcification in vivo

Last, to investigate whether GLS1-mediated glutaminolysis is essential for promoting aortic valve calcification in vivo, we administered vehicle or GLS1 inhibitor, BPTES (10 mg/kg), via intraperitoneal injection in AAC and DWI mice every other day. As expected, after 8 weeks, echocardiography revealed an obvious decrease in transvalvular peak jet velocity and mean gradient in BPTES-treated AAC and DWI mice compared with the vehicle-treated group (Fig. 8, A and B, and figs. S15A and S17A). The cardiac function data were available in figs. S15 (B to F) and S17 (B to F). We observed the restored EF and FS, as well as reduction of LV mass, LVIDd, and LVIDs in BPTES treatment groups compared with AAC and DWI + Vehicle groups, which indicated that BPTES could prevent cardiac remodeling. Besides, BPTES partially prevented AAC- and DWI-induced aortic valve thickness, fibrosis, and calcification (Fig. 8, C to F, and figs. S16, A and B, and S18, A and B) and markedly reduced GLS1 expression (Fig. 8, G to J). Immunofluorescence staining of CD68 showed a reduced invasion of macrophages into valves of the BPTES-treated group compared to AAC and DWI + Vehicle groups (figs. S16C and S18C). Alleviation of aortic valve calcification by BPTES was further confirmed by immunofluorescence for RUNX2 (Fig. 8, K and L). Together, these results implicated that inhibition of GLS1 by BPTES prevented aortic valve calcification.

DISCUSSION

Here, our work provided a cross-talk between Piezo1 activation and glutamine metabolism in CAVD. Piezo1 is essential for identifying various mechanical cues such as fluid flow, stretch/elasticity, and membrane tension in the cardiovascular system. During embryogenesis, Piezo1 was involved in outflow tract and aortic valve

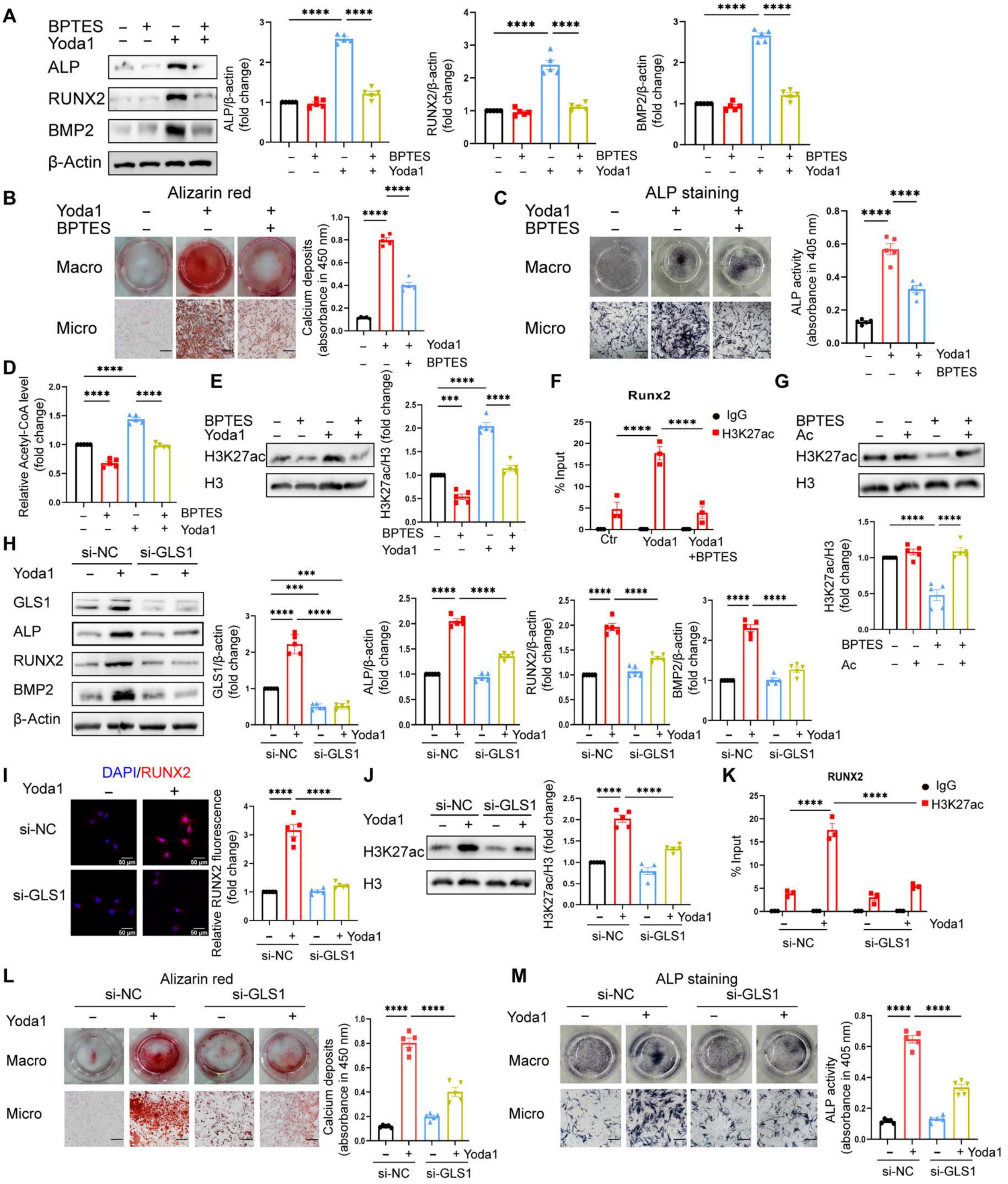

Fig. 7. GLS1-mediated osteogenesis of VICs via histone. (**A**) Representative immunoblots and densitometric data showed that GLS1 inhibitor BPTES markedly reduced Yoda1-induced osteogenic markers in VICs of normal aortic valves; $n = 5$. (**B**) Alizarin red staining of mineralization nodules showed that BPTES treatment significantly reduced Yoda1-induced mineralization nodule formation of normal VICs; $n = 5$; scale bar, 500 μm. (**C**) ALP staining showed that BPTES treatment significantly reduced Yoda1-induced ALP activity of normal VICs; $n = 5$; scale bar, 500 μm. (**D**) Acetyl-CoA concentration in VICs treated with Yoda1 and BPTES; $n = 5$. (**E**) Representative immunoblots and densitometric data showed that GLS1 inhibitor BPTES markedly reduced Yoda1-induced H3K27ac expression; $n = 5$. (**F**) ChIP-PCR showed histone acetylation of RUNX2 promoter regions; $n = 3$. (**G**) Immunoblot of H3K27ac levels in control and BPTES-treated aortic VICs, with or without acetate supplementation; $n = 5$. (**H**) Representative immunoblots and densitometric data showed that GLS1 knockdown markedly reduced Yoda1-induced osteogenic markers; $n = 5$. (**I**) Immunofluorescence staining of RUNX2 in VICs; $n = 5$; scale bar, 50 μm. (**J**) Representative immunoblots and densitometric data showed that, under Yoda1 treatment, aortic VICs with GLS1 knockdown showed reduced expression of H3K27ac compared with scrambled siRNA–transfected VICs of normal aortic valves; $n = 5$. (**K**) ChIP-PCR showed histone acetylation of RUNX2 promoter regions; $n = 3$. (**L**) Alizarin red staining of mineralization nodules showed that GLS1 knockdown significantly reduced Yoda1-induced mineralization nodule formation of VICs of normal aortic valves; $n = 5$; scale bar, 500 μm. (**M**) ALP staining showed that GLS1 knockdown significantly reduced Yoda1-induced ALP activity of normal VICs; $n = 5$; scale bar, 500 μm. Data are means ± SEM. $^{***}P < 0.001$; $^{****}P < 0.0001$; ns, $P > 0.05$.

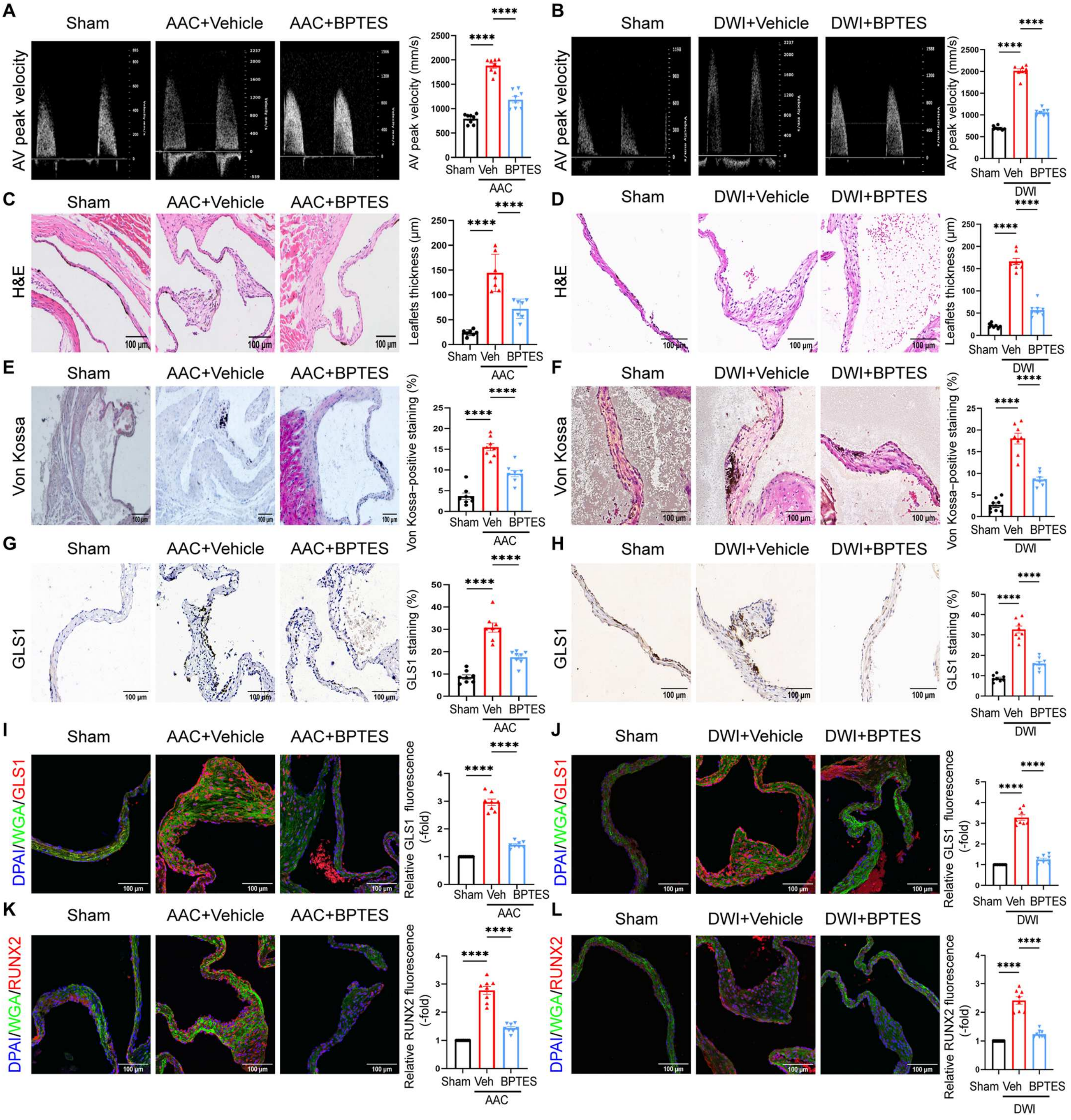

Fig. 8. Inhibition of GLS1 ameliorated aortic valve calcification in vivo. (**A** and **B**) Aortic valve peak velocity of C57BL/6J mice treated with Sham, AAC + Vehicle, and AAC + BPTES ($n = 8$), as well as C57BL/6J mice treated with Sham, DWI + Vehicle, and DWI + BPTES ($n = 8$). (**C** and **D**) H&E staining of mice aortic valve leaflets in AAC-treated mice ($n = 8$) and DWI-treated mice ($n = 8$); scale bar, 100 μm. (**E** and **F**) Representative image of von Kossa staining of mice aortic valve leaflets in AAC-treated mice ($n = 8$) and DWI-treated mice ($n = 8$); scale bar, 100 μm. (**G** and **H**) Representative images of immunohistochemical staining of GLS1 in mice aortic valves from AAC-treated mice ($n = 8$) and DWI-treated mice ($n = 8$); scale bar, 100 μm. (**I** to **L**) Representative images of GLS1 (I) and (J) and RUNX2 (K) and (L) immunofluorescence from AAC-treated mice ($n = 8$) and DWI-treated mice ($n = 8$); scale bar, 100 μm. Data are means ± SEM. ****$P < 0.0001$; ns, $P > 0.05$.

development by regulating Klf2 and Notch activity in the endothelium and YAP localization in smooth muscle progenitors (*30*, *31*). In aortic valve, Piezo1 expression can be found in various cell types, including VICs, the main cell population, endothelial cells, the shield of valve leaflets, as well as infiltrating cells such as monocytes, macrophages, and T lymphocytes. Furthermore, different components of the aortic valve experience different stresses, including high-magnitude steady fluid shear stress on the ventricular surface, oscillatory shear stress on the aortic surface, compressive stress during diastolic pressure loading, and changes in leaflet stiffness. All these stresses may contribute to Piezo1 activation. Baratchi *et al.* (*15*) had reported that patients undergoing TAVR have shown up-regulation of Piezo1 in monocyte populations and high shear stress activation of Piezo1 in monocytes. In this study, we found that Piezo1 expression was up-regulated in the three-layer structure of calcified aortic valve, especially the Spg layer. The endothelium in the aortic side of valve leaflets also highly expressed Piezo1. In regard to that mechanical stimuli may be responsible for increased Piezo1 expression, we tested Piezo1 expression in VICs that responded to LS and OS and found that OS had a greater increase in Piezo1 expression and intercellular Ca^{2+} than LS. Furthermore, Piezo1 activation by its agonist Yoda1 promoted osteogenic differentiation of VICs, which confirmed that Piezo1 activation is necessary for CAVD. Therefore, in CAVD, Piezo1 can be activated by OS and was highly expressed in VICs, valve endothelial cells (VECs) in the aortic side, and the monocytes. One of the limitations of this study is that we focus on the effect of Piezo1 in VICs rather than in VECs. VECs also express Piezo1 and may be involved in inflammation or calcification in aortic valve. However, VICs have a major role in the overall fibrotic and osteogenic response of aortic valve tissue because they are the main cell type within the valve tissue. Another limitation is that we did not conduct all of the mechanical stress experiment in VICs, such as matrix stiffness or compressive stress. These factors may be responsible for Piezo1-mediated aortic calcification. However, in this study, we focused more on the Piezo1-driven mechanisms of mechanoresponse to fluid stress, which coincides with pressure overload created by two CAVD murine models.

Two CAVD murine models are AAC and DWI. It is known that aortic constriction by banding is a common method to induce LV hypertrophy and human aortic stenosis with development of pressure overload–induced LV hypertrophy (*32*). Previous studies have found that constriction of transverse aorta increased Piezo1 expression in cardiomyocytes, resulting in cardiac hypertrophy, while cardiomyocyte-specific deficiency of Piezo1 attenuated pressure overload–induced cardiac hypertrophy, which indicated that Piezo1 is essential for the development of cardiac hypertrophy (*12*, *33*). In this study, we used constriction of ascending aorta because it provides a more direct and higher shear stress overload on the aortic valves. Another CAVD model was constructed by DWI to aortic valve, which has been commonly used to induce valve stenosis (*34*–*37*). It seems that AAC and DWI models present very different pathological and mechanical stresses to the aortic valve. The former creates pressure overload, and the latter causes injury in aortic valve. However, both of them result in the same consequence, which is hemodynamic overload in aortic valve. We observed that both AAC and DWI caused increased aortic velocity and mean gradient, as well as increased aortic valve thickness and Piezo1 expression, which indicated that hemodynamic overload on aortic valve up-regulated Piezo1 and promoted CAVD. Inhibitors of Piezo1, including the ion pore inhibitors ($Gd3^{+}$ and ruthenium red) and the spider toxin GsMTx4, inhibit a range of mechanosensitive ion channels (*38*). Dooku1, despite being less commonly used, has selectivity for Piezo1. It was reported that Dooku1 selectively inhibited the endogenous Piezo1 channel and Yoda1-induced dilation in aorta (*39*). Recent study has also found that application of Dooku1 could inhibit arterial medial calcification (*40*). Therefore, we chose Dooku1 as a useful tool for in vivo study. Unexpectedly, inhibition of Piezo1 by Dooku1 prevented both AAC- and DWI-induced hemodynamic changes and calcification of aortic valve in mice. Several potential mechanisms may be responsible for the Dooku1′s effects seen in these models. First, the mouse models are dependent on Piezo1 activation. Second, inhibition of Piezo1 partially prevented cardiac remodeling, thus leading to relative improved cardiac function and reduced hemodynamic stress. Inhibition of Piezo1 in mice aortic valves reduced the Piezo1-driven mechanoresponse to pressure overload. Therefore, these findings suggested that high shear stress promotes Piezo1 activation and sequent aortic valve calcification, while inhibition of Piezo1 could prevent progression of CAVD.

As a mechanosensitive channel, Piezo1 converts mechanical stimuli into biochemical signals to control cell function (*41*). YAP, known as sensors and mediators of mechanical cues, regulates various aspects of cell behavior, including proliferation, differentiation, and cancer malignant progression (*42*). Multiple evidences have shown that YAP, as a downstream of Piezo1, conducted mechanotransduction signaling for tumor progression and cardiac fibrosis (*43*–*45*). In addition, Santoro *et al.* (*24*) revealed that matrix stiffness by two-dimensional poly-acrylamide gels activated YAP translocation to promote VIC differentiation. Consistently, here, we found that Yoda1 treatment increased the expression and nuclear localization of YAP, and inhibition or knockdown of YAP diminished the pro-osteogenic effect of Yoda1. In fluid stress system, we found that YAP activity was inhibited by LS, which was considered anti-inflammatory and atheroprotective, but promoted by OS. These findings were consistent with previous reports about the role of shear stress in YAP activation (*46*–*48*). Thus, activation of YAP was an important regulatory mechanism of Piezo1-mediated osteogenic differentiation. However, VIC differentiation and YAP activation have been shown to be influenced by substrate stiffness. The substrate we used in cell culture was normal plastic culture dish. Neither VIC differentiation nor YAP activation was found in untreated VICs, as evidenced by Western blot and immunofluorescence staining of YAP. Moreover, the VICs we used were under passage 7, which were unlikely to differentiate. Therefore, we believed that YAP activation was driven by Yoda1-induced Piezo1 activation.

We also observed that the effect of YAP activation was promoted by Yoda1-induced calcium influx. Ca^{2+}, as a secondary message, mediates various signal pathways to maintain homeostasis. Ca^{2+} influx induced by Piezo1 activation has been demonstrated by multiple evidences, which plays a crucial role in pathological condition like cardiac hypertrophy and osteoarthritis (*12*, *49*). In this study, Ca^{2+} signaling induced by Yoda1 was measured using Fluo-4 AM, demonstrating that intracellular Ca^{2+} accumulation was increased by Piezo1 activation. In addition, blocking Ca^{2+} influx with BAPTA-AM reduced intracellular Ca^{2+} concentration and prevented YAP translocation. Together, these findings indicated that

Piezo1 could trigger mechanotransduction signaling in VICs via Ca^{2+} influx-dependent YAP activation.

Here, the identification of GLS1-mediated glutaminolysis as a mechano-activated process advances our understanding of the connection of mechanical stress and metabolic reprogramming in CAVD. Such an interaction between mechanical stress and metabolism has been seen in tumor and pulmonary hypertension. It was reported that matrix stiffness acts as an initiating pathogenic trigger of metabolic changes especially glutaminolysis through YAP mechanoactivation (*20*, *21*). Another mechano-metabolic connection evidence lies on that mechano-induced glutamine metabolism promotes microtubule glutamylation to guide breast cancer metastasis (*50*). Consistent with these findings, our work noted that Piezo1-initiated mechanotransduction promoted glutaminolysis in CAVD. In addition, inhibition or knockdown of YAP abolished the effect of glutaminolysis induced by Yoda1. These findings highlighted the dysregulation of glutaminolysis caused by the Piezo1-YAP axis in CAVD.

Our study then focused on GLS1, a rate-limiting enzyme of glutamine metabolism, which converts glutamine to glutamate. It was reported that GLS1-mediated glutaminolysis was involved in inflammatory response, cardiac fibrosis, as well as chondrocyte and osteogenic gene expression. Arra *et al.* (*51*) noted that glutamine deprivation decreased chondrocyte expression of inflammatory genes in response to interleukin-1β (IL-1β) stimulation. In addition, it has been believed that metabolism has a crucial role in the epigenetic control of genes through certain metabolites (*52*). The glutamine metabolism, for example, generates multiple metabolites such as α-ketoglutaric acid, 2-hydroxyglutarate, and acetyl-CoA, which serve as substrates or cofactors of chromatin-modifying enzymes and play critical roles in mediating epigenetic modification such as methylation and acetylation (*53*). Recently, Xia *et al.* (*54*) identified that acetyl-CoA, generated by GLS1-mediated glutaminolysis, enhanced acetylation of histone 3 in the IL-17A promoter and promoted psoriasis development. Furthermore, Stegen *et al.* (*55*) reported that glutaminolysis controls chondrogenic gene such as aggrecan (ACAN) and collagen 2 (COL2) expression by generating acetyl-CoA synthesis, which is necessary for histone acetylation. In this study, we demonstrated acetyl-CoA as a functional metabolite of glutaminolysis necessary for maintaining acetylation of histone 3 in the RUNX2 promoter. Consistently, we found that GLS1 inhibition decreased osteogenic differentiation in vivo. Together, glutamine metabolism, as downstream of Piezo1-YAP mechanotransduction signaling, regulates VIC osteogenic differentiation through histone acetylation of the promoter region of the osteogenic gene RUNX2, renders the condensed chromatin into a more relaxed state, and thereby promotes calcification.

Although GLS1 inhibitors have been used to suppress various tumor progressions in mice, some of which have entered clinical trial (*56*–*58*), the effect of GLS1 inhibitors in other diseases remained unclear. Recent studies revealed that BPTES treatment (0.25 mg/20 g / 200 μl) of mice ameliorated age-associated disorders (*28*). Here, we used a similar dose (10 mg/kg) of BPTES to treat both AAC and DWI mice and observed that BPTES ameliorated aortic valve calcification in mice. Therefore, our findings indicate that the GLS1 inhibitor BPTES is an attractive potential drug for the treatment of CAVD.

In conclusion, the present study provided evidence that activation of Piezo1 as an initial pathologic trigger promoted stress-induced osteogenic differentiation of VICs through YAP-dependent glutaminolysis. Glutaminolysis then promotes osteogenic gene expression through histone acetylation, thereby causing the development of CAVD (Fig. 9). Together, our study uncovered the interface of Piezo1-mediated mechanotransduction with GLS1-mediated glutaminolysis in the context of CAVD.

MATERIALS AND METHODS

Human sample collection

Calcified aortic valve tissues were obtained from patients undergoing aortic valve replacement. Control samples (without calcified aortic valve tissue) were collected from the explanted hearts of patients undergoing heart transplantation ($n = 10$). Aortic valve tissues were washed with phosphate-buffered saline (PBS) buffer in clean bench and then divided into three parts: One part was quickly frozen with liquid nitrogen and then stored at −80°C, which can be used for tissue protein and RNA extraction; another part was fixed in 4% paraformaldehyde for tissue slice; the last one was used to separate VICs. Peripheral venous plasma were collected from CAVD patients and non-CAVD patients. The exclusion criteria included infective endocarditis, congenital valve disease, rheumatic heart disease, and autoimmune diseases. CAVD was diagnosed when the leaflet thickness was ≥3 mm, the aortic valve (AV) peak velocity was ≥1.5 m/s, and there was increased echogenicity (aortic root echogenicity was the control) (*59*). Informed consent was obtained from all patients. The protocol of this study was conducted in accordance with the Declaration of Helsinki and was approved by the Nanfang Hospital, Southern Medical University. The cohort study was registered in the Chinese Clinical Trial Registry (www.chictr.org.cn, ChiCTR-ROC-17011240).

Animal experiments and echocardiography assessment

The animal study was approved by the Ethics Review Committee of Southern Medical University (NFYY-2021-0437). All mice were maintained in a light/dark cycle of 12 hours/12 hours at a temperature of 21°C and 50% humidity. AAC was performed under anesthesia in 12-week-old, male, C57BL/6J mice, weighing between 25 and 30 g. In these mice, constriction of the ascending aorta was performed with a 24-gauge needle, as previously described (*60*, *61*). Sham operation was performed under the same conditions except for the aortic banding. All mice were fed normal chow during the whole experiment.

DWI mouse model was conducted in 12-week-old, male, C57BL/6J mice as previously described with minor modifications (*34*, *62*). Briefly, a spring wire for angioplasty was introduced into the right carotid artery in the mouse. After the wire was inserted into the ascending aorta, we slowly rotated and carefully inserted it into the left ventricle. Aortic valve injury was induced by scratching the leaflets with the body of the wire for 50 times and spinning the tip of the wire correctly positioned on the LV side of the valve for 100 times (fig. S5A). After the wire was removed, the right carotid artery was ligated. Sham surgery was performed in the same way but without wire insertion into the left ventricle. All mice were fed normal chow during the whole experiment.

Inhibition of Piezo1 in mice

Randomization was ensured by arbitrarily assigning models to Dooku1 or vehicle treatment. Dooku1 (10 mg/kg; Selleck, USA)

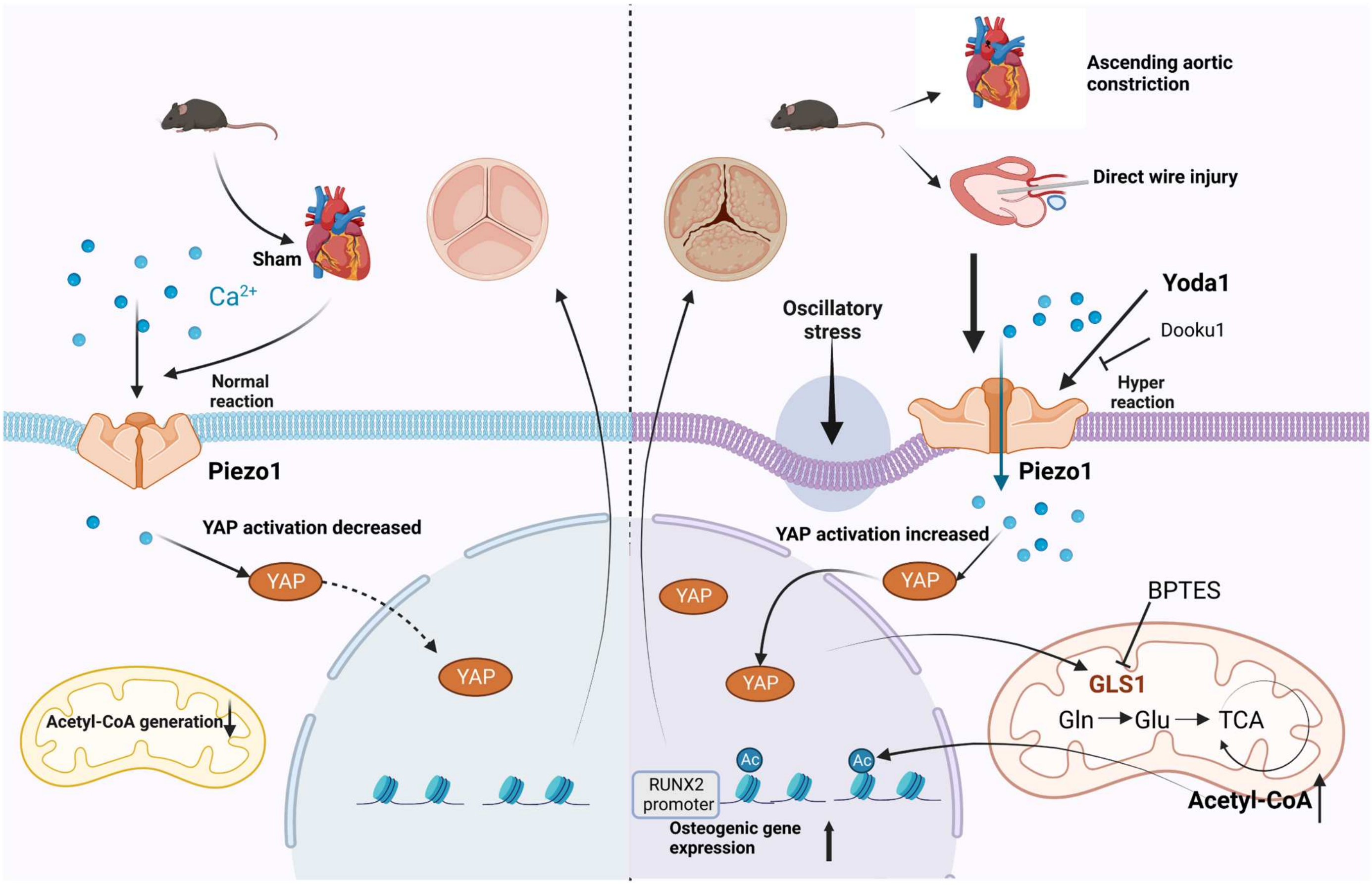

Fig. 9. Schematic illustration of Piezo1-YAP mechanotransduction-mediated glutaminolysis contributing to the pathogenesis of CAVD. High shear stress in vivo and Yoda1 treatment in vitro caused Piezo1 activation. Piezo1 activation triggered increased Ca^{2+} influx and YAP translocation, which further promoted GLS1-mediated glutaminolysis. Glutaminolysis augments intracellular acetyl-CoA, which contributes to histone H3 acetylation of the osteogenic marker RUNX2 promoter, thereby aggravating development of CAVD.

was applied via intraperitoneal injection every other day. PBS was used as a vehicle control.

Inhibition of GLS1 in mice

Randomization was ensured by arbitrarily assigning models to BPTES or vehicle treatment. GLS1 (10 mg/kg; Selleck, USA) was applied via intraperitoneal injection every other day. PBS was used as a vehicle control.

After 8 weeks, hemodynamic parameters were determined to verify aortic constriction by transthoracic echocardiography using a Vevo 2100 imaging system under 2.5% isoflurane anesthesia. After that, the mice were euthanized by intravenous injection of a lethal dose of pentobarbital sodium (100 mg/kg). Mice were then perfused via the left ventricle with 5 ml of PBS before tissue collection. The heart tissues were embedded in paraffin and dissected into 5-μm sections. The sections were fixed in 4% paraformaldehyde for H&E staining, von Kossa staining, immunohistochemical staining, and immunofluorescence staining.

Targeted LC-MS/MS

Metabolite extraction was performed essentially as described with minor modifications (*63*). Briefly, metabolites were extracted from plasma precleared by centrifugation at 20,000*g* for 10 min at 4°C. Then, enough volumes of 100% methanol were added and precooled at −80°C overnight. The supernatant was collected in a Speedvac (Acid-Resistant CentriVap Vacuum Concentrators, Labconco) after centrifugation at 20,000*g* for 20 min at 4°C and then analyzed by Prelude SPLC+TSQ Quantiva LC-MS/MS (Thermo Scientific, USA). The MS parameters were optimized using targeted metabolite standards (Solarbio, China), which were L-glutamine (SG8550), L-glutamate (SG8540), L-aspartate (SA8560), and pyruvate (SP9670). Mass transitions and retention time windows were confirmed by the analysis of neat and matrix-spiked standards. Peak areas and calculated amount were quantified by Xcalibur software (Thermo Fisher Scientific, USA) and manually reviewed.

Primary cell isolation and culture and treatment

Primary aortic VICs were isolated from human aortic valves by using a well-established method with modifications (*64*). The leaflets were washed with ice-cold PBS and digested in medium containing collagenase (type II, 2.5 mg/ml; Sigma-Aldrich, 1148090, USA) at 37°C for 30 min to remove valve endothelial cells. The remaining valve tissues were cut into pieces and further digested with a fresh solution of collagenase (0.8 mg/ml) in medium for 4 to 6 hours at 37°C. Interstitial cells were collected and cultured in

Dulbecco's modified Eagle's medium and 10% fetal bovine serum at 37°C in an atmosphere of 5% carbon dioxide. The substrate we used in cell culture was normal plastic culture dish (Corning, USA). VICs at passages 3 to 6 were used in subsequent experiments.

To determine the effect of Piezo1 on the expression of ALP, RUNX2, and BMP2, VICs were treated with Yoda1 (Selleck, USA) (0, 2.5, 5, and 10 μM) for 24 hours. We chose 5 μM Yoda1 for Piezo1 activation in the study. For the inhibition treatments, cells were respectively treated with 2.5 and 5 μM Dooku1 (Selleck, USA), 1 μM verteporfin (Selleck, USA), 10 μM BAPTA-AM (APExBIO, USA), and 5 μM BPTES (Selleck, USA). Rescue experiments with sodium acetate (Sigma-Aldrich, USA) were performed at 1 mM.

The flow experiments were performed as previously described (*46*). VICs within passages 4 and 6 were seeded onto μ-Slide I Luer (Ibidi, Germany) and grown until confluence. A parallel plate flow system (Ibidi, Germany) was used to impose oscillatory flow (0.5 ± 4 dynes/cm^2) or laminar flow (12 dynes/cm^2). The flow system was enclosed in a chamber held at 37°C and ventilated with 95% humidified air plus 5% CO_2.

Cell transfection of siRNAs

To knock down Piezo1, cells (70 to 80% confluent) in six-well plates were incubated with a mixture of Piezo1 siRNA (100 nM), Lipofectamine 3000, and Opti-MEM for 48 hours, and then cell stimulation was performed. Control cells were treated with scrambled siRNA and transfection reagent. YAP and GLS1 silencing were performed using the method described above. siRNA for Piezo1 and GLS1 was designed and provided by Tsingke, China, and YAP siRNA was from RiboBio, China.

Nuclear and cytoplasmic protein extraction

The nuclear and cytoplasmic protein components of aortic VICs were isolated using NEPER nuclear and cytoplasmic extraction reagents (Thermo Fisher Scientific, USA) according to the manufacturer's protocol. Glyceraldehyde-3-phosphate dehydrogenase (GAPDH) or histone 3 (H3) served as controls for the cytoplasmic or nuclear protein components, respectively.

Immunoblot

Human aortic valve samples were cut and added with radioimmunoprecipitation assay (RIPA) lysis (100 mg:1 ml) containing phosphatase and protease inhibitors (1:100) to homogenize. Then, the sample was centrifuged at 12,000*g* for 15 min to pellet tissue debris. Supernatant was collected and prepared for immunoblot. VICs were lysed in lysis buffer (Beyotime Institute of Biotechnology, China) containing phosphatase and protease inhibitors (1:100) and quantified with a bicinchoninic acid protein assay. Protein samples were separated on SDS–polyacrylamide gels (Epizyme, China) and transferred to polyvinylidene fluoride membranes (EMDMillipore, Billerica, MA, USA). The membranes were blocked with 5% nonfat powdered milk solution for 1 hour at room temperature. The blocked membranes were incubated overnight at 4°C with a primary antibody. The membranes were subsequently incubated with a horseradish peroxidase (HRP)–conjugated secondary antibody specific to the primary antibody. Immunoreactive bands were detected with Pierce enhanced chemiluminescence substrate (Pierce; Thermo Fisher Scientific Inc.) and a GeneGnome imaging system (Syngene, Frederick, MD, USA). ImageJ was used to determine the band density. The primary antibodies used in our study include Piezo1 antibody (1:1000; Proteintech, 15939-1-AP, China), β-actin antibody (1:4000; Beijing Ray Antibody Biotech, RM2001, China), ALP antibody (1:1000; ABclonal, A0514, China), RUNX2 antibody (1:1000; Proteintech, 20700-1-AP, China), BMP2 antibody (1:1000; Abcam, ab284395, USA), YAP antibody (1:1000; ABclonal, A1002, China), p-YAP-S127 (1:1000; ABclonal, AP0489, China), GLS1(1:1000; Abmart, T55719, China), H3K27Ac (1:1000; Abcam, ab177178, USA), and α-SMA (1:1000; Abcam, ab124964, USA). Goat anti-rabbit HRP-conjugated antibody (1:5000; FUDE Biological Technology, FDR007, China) and goat anti-mouse HRP-conjugated antibody (1:5000; FUDE Biological Technology, FDM007, China) were used as secondary antibodies.

Alizarin red S staining

When reaching 80% confluence, VICs were incubated with indicated interventions in an osteogenic medium [growth medium supplemented with β-glycerophosphate (10 mM), dexamethasone (10 nM), cholecalciferol (4 μg/ml), and $CaCl_2$ (8 mM)] for 21 days. The medium was changed every 3 days. Alizarin red S staining for calcium deposits was performed as previously described (*65*). Briefly, cell monolayers were washed three times with PBS and fixed for 15 min in 4% paraformaldehyde, followed by incubation with 0.2% alizarin red solution (pH 4.2) for 30 min. Excessive dye was removed by washing with distilled water. Alizarin red staining was examined and photographed with an OLYMPUS CKX41 microscope (Japan). For quantitation, the stain was washed off with 10% acetic acid at 75°C and measured using a spectrophotometer at 450-nm wavelength.

ALP activity

ALP staining for ALP formation was performed by using BCIP/NBT Alkaline Phosphatase Color Development Kit (Beyotime, China) according to the manufacturer's protocols. Briefly, VICs were washed three times with PBS and fixed for 15 min in 4% paraformaldehyde, followed by incubation with Alkaline Phosphatase Color Solution for 2 hours. Excessive dye was removed by washing with distilled water. VICs were examined and photographed with an OLYMPUS CKX41 microscope (Japan). ALP activity quantitation was performed by using an alkaline phosphatase detection kit (Beyotime, China) according to the manufacturer's protocols. Briefly, VICs were lysed with lysis buffer. The lysates were spun at 8000*g* for 10 min at 4°C, and the supernatants were then incubated with chromogenic substrate at 37°C for 30 min. ALP activity was measured with the absorbance at 405 nm.

Histological and immunohistochemical assay

Paraffin-embedded aortic valve samples were cut into 5-mm-thick sections and then incubated for 2 hours at 72°C before being deparaffinized with xylene and alcohol. H&E-stained sections were examined to identify the differences between noncalcified and calcified aortic valves. Immunohistochemistry detection of Piezo1 and GLS1 in mouse aortic valve leaflets was performed. For immunohistochemistry, after antigen retrieval was performed with a microwave, the prepared sections were incubated in 3% H_2O_2 for 10 min. Then, the sections were rinsed with PBS and blocked in 5% bovine serum albumin for 30 min at room temperature, followed by incubation with primary antibodies overnight at 4°C and

HRP-conjugated secondary antibodies for 30 min at room temperature. Then, diaminobenzidine was used as a chromogen to visualize positive cells. The primary antibodies we used in immunohistochemistry staining were Piezo1 (1:100; Proteintech, 15939-1-AP, China) and GLS1 (1:100; Abmart, T55719, China). The secondary antibody was goat anti-rabbit HRP-conjugated antibody (1:200; FUDE Biological Technology, FDR007, China).

The deparaffinized and rehydrated sections were stained with von Kossa solution and alizarin red staining (Solarbio, China) to detect calcium deposits. Masson's trichrome staining was performed to detect collagen deposition.

Immunofluorescence staining

Immunofluorescence detection of Piezo1, GLS1, Runx2, vimentin, CD68, and CD31 in mouse aortic valve leaflets was performed. Tissue sections were fixed in 4% paraformaldehyde and incubated with primary antibodies overnight at 4°C. After being washed with PBS, the sections were incubated with Alexa Fluor 594–conjugated secondary antibodies (red channel). Nuclei were stained with 4′,6-diamidino-2-phenylindole (DAPI; blue channel), and glycoproteins on cell surfaces were stained with Alexa Fluor 488–conjugated wheat germ agglutinin (green channel). Microscopy was performed with Leica SP8. The method of VIC immunofluorescence staining is similar. Briefly, VICs were fixed in 4% paraformaldehyde and permeabilized in 0.2% Triton X-100. Then, the cells were blocked for 15 min and incubated with primary antibodies overnight at 4°C. After washing with PBS, cells were incubated with a goat anti-rabbit secondary antibody against the primary antibody. Nuclei were stained with DAPI. Confocal images were acquired using Leica SP8. The primary antibodies we used in immunofluorescence staining were the following: Piezo1 (1:100; Abmart, M25233, China), GLS1 (1:100; Abmart, T55719, China), RUNX2 (1:100; Abcam, ab76956, USA), vimentin (1:100; Proteintech, 60330-1-Ig, China), CD68 (1:100; Abcam, ab283654, USA), and CD31 (1:100; Affinity, AF6191, USA). The secondary antibodies we used were the following: goat anti-rabbit IgG H&L (Alexa Fluor 488) (1:200; Abcam, ab150077, USA), goat anti-rabbit IgG H&L (Alexa Fluor 594) (1:200; Abcam, ab150080, USA), goat anti-mouse IgG H&L/Cy3 (1:200; Bioss, bs-0296G-Cy3, China), and goat anti-mouse IgG H&L/AF488 antibody (1:200; Bioss, bs-0296G-AF488, China).

Calcium imaging

VICs were incubated with Fluo-4 AM (5 μM; Beyotime, China) according to the manufacturer's protocols. VICs were then washed by Hanks' balanced salt solution and placed at 37°C in 5% CO_2 for 10 min. Imaging was performed by using a Leica SP8 scanning microscope.

Metabolite detection

Glutamate concentration was analyzed using the Glutamate Assay Kit (Mlbio, China) following the manufacturer's instructions. In general, 1×10^6 cells were homogenized in the Glutamate Assay Buffer followed by centrifugation. The supernatants were mixed with Buffer 2, a color reagent. After incubating the reaction for 20 min at 90°C, the absorbance was measured at 570 nm. All samples and standards were run in duplicate.

Glutamine concentration was analyzed using a glutamine assay kit (Mlbio, China) following the manufacturer's instructions. In general, 1×10^6 cells were homogenized in the glutamine assay buffer followed by centrifugation. The supernatants were then mixed with a series of reagents to the reaction. After incubating the reaction for 30 min at 37°C in the dark, the absorbance was measured at 450 nm. All samples and standards were run in duplicate.

The measurement of cytosolic acetyl-CoA was analyzed using an acetyl-CoA assay kit (Bioss, China) following the manufacturer's instructions. In general, 1×10^6 cells were lysed with lysis buffer on ice for 10 min. The lysates were spun at 8000*g* for 10 min at 4°C, and the supernatants were used for acetyl-CoA measurement with the absorbance at 340 nm.

Reverse transcription and qPCR analyses

Total RNA was extracted with RNA isolator total RNA extraction reagent (Vazyme, R401-01, China) according to the manufacturer's instructions. Briefly, 1 ml of total RNA extraction reagent per 50 to 100 mg of tissue was added to the sample or cells (1×10^5 to 1×10^7), and the mixture was homogenized using a homogenizer. Then, 0.2 ml of chloroform was added per 1 ml of TRIzol reagent used for lysis, and the mixture was incubated for 5 min. The sample was centrifuged for 15 min at 12,000*g* at 4°C. The mixture separates into a lower red phenol-chloroform, an interphase, and a colorless upper aqueous phase. The aqueous phase containing the RNA was transferred to a new tube. Then, the RNA was precipitated with isopropanol, washed with 75% ethanol, and solubilized with RNA-free water. RNA samples were reverse-transcribed using the HiScript II Q RT SuperMix for qPCR (+gDNA wiper) (Vazyme, R223-01, China). Relative mRNA levels were determined by real-time PCR using Taq Pro Universal SYBR qPCR Master Mix (Vazyme, R712-02, China) and a real-time PCR detection system (LightCycler 480, Roche, USA). The results are expressed as Ct values normalized to 18S, and the fold change between the control and treated groups was determined using the $2^{-\Delta\Delta Ct}$ method.

The following primers were used: *PIEZO1*-F, CCTGTCCGCCTACCAGATCCG; *PIEZO1*-R, ACCCATGCCGTACTTGACGAT; *PIEZO2*-F, ACTCTTTGGATGATTCGCAAC; *PIEZO2*-R, CTGCCAATTTTGACTTCCGAT; *GLS*-F, ATCTACAGGATTGCGAACGTCT; *GLS*-R, AATCTTAGTCCACTCGGCTCT; *18S*-F, TAGAGGGACAAGTGGCGT; and *18S*-R, AATGGGGTTCAACGGGTT.

ChIP-qPCR

ChIP-qPCR was performed using a ChIP kit (Bersinbio, bes5001, China) as described in the manufacturer's instructions. Briefly, VICs were fixed using 1% formaldehyde, washed, and collected by centrifugation (1000*g* for 5 min at 4°C). The pellet was resuspended in lysis buffer with 1% protease inhibitors and dithiothreitol, homogenized, incubated on ice for 10 min, and sonicated. The samples were centrifuged (13,000*g* for 10 min at 4°C), and shared chromatin was used as input and incubated with an anti-H3K27Ac antibody (Abcam, USA). Rabbit IgG (Abcam, USA) was used as isotype control. After precipitation using Pierce Protein A/G Magnetic Beads, followed by RNA and protein digestion, DNA was purified according to the manufacturer's instructions. RT-qPCR was performed using SYBR GreenER qPCR SuperMix Universal (Vazyme, China). The qPCR primers used to evaluate the promoter regions were as follows: RUNX2 Fw, GTGGTAGGCAGTCCCACTTTA; RUNX2 Rev, AGAAAGTTTGCACCGCACTTG.

Statistical analysis

The continuous data are presented as means ± SEM. A normal distribution test was performed to determine whether a parametric or nonparametric test was conducted. Comparisons between multiple groups were analyzed using one-way or two-way analysis of variance (ANOVA) with a post hoc Bonferroni/Dunn test, and two-group comparisons were analyzed using Student's t test. The statistical analyses were performed using GraphPad Prism 9.0. Statistical significance was defined as $P \leq 0.05$.

Supplementary Materials

This PDF file includes:

Figs. S1 to S18
Tables S1 and S2

View/request a protocol for this paper from *Bio-protocol*.

REFERENCES AND NOTES

1. S. Coffey, B. Cox, M. J. Williams, The prevalence, incidence, progression, and risks of aortic valve sclerosis: A systematic review and meta-analysis. *J. Am. Coll. Cardiol.* **63**, 2852–2861 (2014).
2. B. R. Lindman, M. A. Clavel, P. Mathieu, B. Iung, P. Lancellotti, C. M. Otto, P. Pibarot, Calcific aortic stenosis. *Nat. Rev. Dis. Primers.* **2**, 16006 (2016).
3. C. M. Otto, R. A. Nishimura, R. O. Bonow, B. A. Carabello, J. R. Erwin, F. Gentile, H. Jneid, E. V. Krieger, M. Mack, C. Mcleod, P. T. O'Gara, V. H. Rigolin, T. R. Sundt, A. Thompson, C. Toly, 2020 ACC/AHA guideline for the management of patients with valvular heart disease: Executive summary: A report of the american college of cardiology/american heart association joint committee on clinical practice guidelines. *J. Am. Coll. Cardiol.* **77**, 450–500 (2021).
4. S. Baratchi, K. Khoshmanesh, O. L. Woodman, S. Potocnik, K. Peter, P. Mcintyre, Molecular sensors of blood flow in endothelial cells. *Trends Mol. Med.* **23**, 850–868 (2017).
5. M. Mohammed, P. Thurgood, C. Gilliam, N. Nguyen, E. Pirogova, K. Peter, K. Khoshmanesh, S. Baratchi, Studying the response of aortic endothelial cells under pulsatile flow using a compact microfluidic system. *Anal. Chem.* **91**, 12077–12084 (2019).
6. F. Lassalle, M. Rosa, B. Staels, E. Van Belle, S. Susen, A. Dupont, Circulating monocyte subsets and transcatheter aortic valve replacement. *Int. J. Mol. Sci.* **23**, 5303 (2022).
7. C. Y. Y. Yip, J. Chen, R. Zhao, C. A. Simmons, Calcification by valve interstitial cells is regulated by the stiffness of the extracellular matrix. *Arterioscler. Thromb. Vasc. Biol.* **29**, 936–942 (2009).
8. A. M. T. Quinlan, K. L. Billiar, Investigating the role of substrate stiffness in the persistence of valvular interstitial cell activation. *J. Biomed. Mater. Res. Part A* **100A**, 2474–2482 (2012).
9. M. Pho, W. Lee, D. R. Watt, C. Laschinger, C. A. Simmons, C. A. Mcculloch, Cofilin is a marker of myofibroblast differentiation in cells from porcine aortic cardiac valves. *Am. J. Physiol. Heart Circul. Physiol.* **294**, H1767–H1778 (2008).
10. B. Coste, J. Mathur, M. Schmidt, T. J. Earley, S. Ranade, M. J. Petrus, A. E. Dubin, A. Patapoutian, Piezo1 and Piezo2 are essential components of distinct mechanically activated cation channels. *Science* **330**, 55–60 (2010).
11. K. Saotome, S. E. Murthy, J. M. Kefauver, T. Whitwam, A. Patapoutian, A. B. Ward, Structure of the mechanically activated ion channel Piezo1. *Nature* **554**, 481–486 (2018).
12. Y. Zhang, S. A. Su, W. Li, Y. Ma, J. Shen, Y. Wang, Y. Shen, J. Chen, Y. Ji, Y. Xie, H. Ma, M. Xiang, Piezo1-mediated mechanotransduction promotes cardiac hypertrophy by impairing calcium homeostasis to activate calpain/calcineurin signaling. *Hypertension* **78**, 647–660 (2021).
13. D. J. Beech, A. C. Kalli, Force sensing by piezo channels in cardiovascular health and disease. *Arterioscler. Thromb. Vasc. Biol.* **39**, 2228–2239 (2019).
14. J. Li, B. Hou, S. Tumova, K. Muraki, A. Bruns, M. J. Ludlow, A. Sedo, A. J. Hyman, L. Mckeown, R. S. Young, N. Y. Yuldasheva, Y. Majeed, L. A. Wilson, B. Rode, M. A. Bailey, H. R. Kim, Z. Fu, D. A. Carter, J. Bilton, H. Imrie, P. Ajuh, T. N. Dear, R. M. Cubbon, M. T. Kearney, R. K. Prasad, P. C. Evans, J. F. Ainscough, D. J. Beech, Piezo1 integration of vascular architecture with physiological force. *Nature* **515**, 279–282 (2014).
15. S. Baratchi, M. Zaldivia, M. Wallert, J. Loseff-Silver, S. Al-Aryahi, J. Zamani, P. Thurgood, A. Salim, N. M. Htun, D. Stub, P. Vahidi, S. J. Duffy, A. Walton, T. H. Nguyen, A. Jaworowski, K. Khoshmanesh, K. Peter, Transcatheter aortic valve implantation represents an anti-inflammatory therapy via reduction of shear stress-induced, Piezo-1-mediated monocyte activation. *Circulation* **142**, 1092–1105 (2020).
16. R. Syeda, J. Xu, A. E. Dubin, B. Coste, J. Mathur, T. Huynh, J. Matzen, J. Lao, D. C. Tully, I. H. Engels, H. M. Petrassi, A. M. Schumacher, M. Montal, M. Bandell, A. Patapoutian, Chemical activation of the mechanotransduction channel Piezo1. *eLife* **4**, e07369 (2015).
17. W. M. Botello-Smith, W. Jiang, H. Zhang, A. D. Ozkan, Y. C. Lin, C. N. Pham, J. J. Lacroix, Y. Luo, A mechanism for the activation of the mechanosensitive Piezo1 channel by the small molecule Yoda1. *Nat. Commun.* **10**, 4503 (2019).
18. K. Retailleau, F. Duprat, M. Arhatte, S. S. Ranade, R. Peyronnet, J. R. Martins, M. Jodar, C. Moro, S. Offermanns, Y. Feng, S. Demolombe, A. Patel, E. Honoré, Piezo1 in smooth muscle cells is involved in hypertension-dependent arterial remodeling. *Cell Rep.* **13**, 1161–1171 (2015).
19. S. Leng, X. Zhang, S. Wang, J. Qin, Q. Liu, A. Liu, Z. Sheng, Q. Feng, X. Hu, J. Peng, Ion channel Piezo1 activation promotes aerobic glycolysis in macrophages. *Front. Immunol.* **13**, 976482 (2022).
20. T. Bertero, W. M. Oldham, K. A. Cottrill, S. Pisano, R. R. Vanderpool, Q. Yu, J. Zhao, Y. Tai, Y. Tang, Y. Y. Zhang, S. Rehman, M. Sugahara, Z. Qi, J. R. Gorcsan, S. O. Vargas, R. Saggar, R. Saggar, W. D. Wallace, D. J. Ross, K. J. Haley, A. B. Waxman, V. N. Parikh, T. De Marco, P. Y. Hsue, A. Morris, M. A. Simon, K. A. Norris, C. Gaggioli, J. Loscalzo, J. Fessel, S. Y. Chan, Vascular stiffness mechanoactivates YAP/TAZ-dependent glutaminolysis to drive pulmonary hypertension. *J. Clin. Invest.* **126**, 3313–3335 (2016).
21. T. Bertero, W. M. Oldham, E. M. Grasset, I. Bourget, E. Boulter, S. Pisano, P. Hofman, F. Bellvert, G. Meneguzzi, D. V. Bulavin, S. Estrach, C. C. Feral, S. Y. Chan, A. Bozec, C. Gaggioli, Tumor-stroma mechanics coordinate amino acid availability to sustain tumor growth and malignancy. *Cell Metab.* **29**, 124–140.e10 (2019).
22. G. Santinon, I. Brian, A. Pocaterra, P. Romani, E. Franzolin, C. Rampazzo, S. Bicciato, S. Dupont, dNTP metabolism links mechanical cues and YAP/TAZ to cell growth and oncogene-induced senescence. *EMBO J.* **37**, e97780 (2018).
23. F. X. Yu, B. Zhao, K. L. Guan, Hippo pathway in organ size control, tissue homeostasis, and cancer. *Cell* **163**, 811–828 (2015).
24. R. Santoro, D. Scaini, L. U. Severino, F. Amadeo, S. Ferrari, G. Bernava, G. Garoffolo, M. Agrifoglio, L. Casalis, M. Pesce, Activation of human aortic valve interstitial cells by local stiffness involves YAP-dependent transcriptional signaling. *Biomaterials* **181**, 268–279 (2018).
25. H. Ma, A. R. Killaars, F. W. Delrio, C. Yang, K. S. Anseth, Myofibroblastic activation of valvular interstitial cells is modulated by spatial variations in matrix elasticity and its organization. *Biomaterials* **131**, 131–144 (2017).
26. A. A. Gibb, E. K. Murray, A. T. Huynh, R. B. Gaspar, T. L. Ploesch, K. Bedi, A. A. Lombardi, P. K. Lorkiewicz, R. Roy, Z. Arany, D. P. Kelly, K. B. Margulies, B. G. Hill, J. W. Elrod, Glutaminolysis is essential for myofibroblast persistence and in vivo targeting reverses fibrosis and cardiac dysfunction in heart failure. *Circulation* **145**, 1625–1628 (2022).
27. A. A. Gibb, A. T. Huynh, R. B. Gaspar, T. L. Ploesch, A. A. Lombardi, P. K. Lorkiewicz, M. P. Lazaropoulos, K. Bedi, Z. Arany, K. B. Margulies, B. G. Hill, J. W. Elrod, Glutamine uptake and catabolism is required for myofibroblast formation and persistence. *J. Mol. Cell. Cardiol.* **172**, 78–89 (2022).
28. Y. Johmura, T. Yamanaka, S. Omori, T. W. Wang, Y. Sugiura, M. Matsumoto, N. Suzuki, S. Kumamoto, K. Yamaguchi, S. Hatakeyama, T. Takami, R. Yamaguchi, E. Shimizu, K. Ikeda, N. Okahashi, R. Mikawa, M. Suematsu, M. Arita, M. Sugimoto, K. I. Nakayama, Y. Furukawa, S. Imoto, M. Nakanishi, Senolysis by glutaminolysis inhibition ameliorates various age-associated disorders. *Science* **371**, 265–270 (2021).
29. B. R. Sabari, D. Zhang, C. D. Allis, Y. Zhao, Metabolic regulation of gene expression through histone acylations. *Nat. Rev. Mol. Cell Biol.* **18**, 90–101 (2017).
30. A. L. Duchemin, H. Vignes, J. Vermot, Mechanically activated piezo channels modulate outflow tract valve development through the Yap1 and Klf2-Notch signaling axis. *eLife* **8**, e44706 (2019).
31. A. Faucherre, O. M. H. Moha, N. Nasr, A. Pinard, A. Theron, G. Odelin, J. P. Desvignes, D. Salgado, G. Collod-Béroud, J. F. Avierinos, G. Lebon, S. Zaffran, C. Jopling, Piezo1 is required for outflow tract and aortic valve development. *J. Mol. Cell. Cardiol.* **143**, 51–62 (2020).
32. O. Tarnavski, J. R. Mcmullen, M. Schinke, Q. Nie, S. Kong, S. Izumo, Mouse cardiac surgery: Comprehensive techniques for the generation of mouse models of human diseases and their application for genomic studies. *Physiol. Genomics* **16**, 349–360 (2004).
33. Z. Yu, H. Gong, S. Kesteven, Y. Guo, J. Wu, J. V. Li, D. Cheng, Z. Zhou, S. E. Iismaa, X. Kaidonis, R. M. Graham, C. D. Cox, M. P. Feneley, B. Martinac, Piezo1 is the cardiac mechanosensor that initiates the cardiomyocyte hypertrophic response to pressure overload in adult mice. *Nat. Cardiovasc. Res.* **1**, 577–591 (2022).
34. S. Honda, T. Miyamoto, T. Watanabe, T. Narumi, S. Kadowaki, Y. Honda, Y. Otaki, H. Hasegawa, S. Netsu, A. Funayama, M. Ishino, S. Nishiyama, H. Takahashi, T. Arimoto, T. Shishido, T. Miyashita, I. Kubota, A novel mouse model of aortic valve stenosis induced by direct wire injury. *Arterioscler. Thromb. Vasc. Biol.* **34**, 270–278 (2014).
35. S. T. Niepmann, N. Willemsen, A. S. Boucher, M. Stei, P. Goody, A. Zietzer, M. Bulic, H. Billig, A. Odainic, C. K. Weisheit, C. Quast, M. Adam, S. V. Schmidt, F. Bakhtiary, F. Jansen,

G. Nickenig, E. Latz, S. Zimmer, Toll-like receptor-3 contributes to the development of aortic valve stenosis. *Basic Res. Cardiol.* **118**, 6 (2023).

36. F. Iqbal, F. Schlotter, D. Becker-Greene, A. Lupieri, C. Goettsch, J. D. Hutcheson, M. A. Rogers, S. Itoh, A. Halu, L. H. Lee, M. C. Blaser, A. K. Mlynarchik, S. Hagita, S. Kuraoka, H. Y. Chen, J. C. Engert, L. Passos, P. K. Jha, E. A. Osborn, F. A. Jaffer, S. C. Body, S. C. Robson, G. Thanassoulis, M. Aikawa, S. A. Singh, A. R. Sonawane, E. Aikawa, Sortilin enhances fibrosis and calcification in aortic valve disease by inducing interstitial cell heterogeneity. *Eur. Heart J.* **44**, 885–898 (2023).
37. F. Liu, J. Chen, W. Hu, C. Gao, Z. Zeng, S. Cheng, K. Yu, Y. Qian, D. Xu, G. Zhu, J. Zhao, X. Liu, J. Wang, PTP1B inhibition improves mitochondrial dynamics to alleviate calcific aortic valve disease via regulating OPA1 homeostasis. *JACC Basic Transl. Sci.* **7**, 697–712 (2022).
38. C. Bae, F. Sachs, P. A. Gottlieb, The mechanosensitive ion channel Piezo1 is inhibited by the peptide GsMTx4. *Biochemistry* **50**, 6295–6300 (2011).
39. E. L. Evans, K. Cuthbertson, N. Endesh, B. Rode, N. M. Blythe, A. J. Hyman, S. J. Hall, H. J. Gaunt, M. J. Ludlow, R. Foster, D. J. Beech, Yoda1 analogue (Dooku1) which antagonizes Yoda1-evoked activation of Piezo1 and aortic relaxation. *Br. J. Pharmacol.* **175**, 1744–1759 (2018).
40. L. Szabó, N. Balogh, A. Tóth, Á. Angyal, M. Gönczi, D. M. Csiki, C. Tóth, I. Balatoni, V. Jeney, L. Csernoch, B. Dienes, The mechanosensitive Piezo1 channels contribute to the arterial medial calcification. *Front. Physiol.* **13**, 1037230 (2022).
41. F. Jiang, K. Yin, K. Wu, M. Zhang, S. Wang, H. Cheng, Z. Zhou, B. Xiao, The mechanosensitive Piezo1 channel mediates heart mechano-chemo transduction. *Nat. Commun.* **12**, 869 (2021).
42. S. Dupont, L. Morsut, M. Aragona, E. Enzo, S. Giulitti, M. Cordenonsi, F. Zanconato, J. Le Digabel, M. Forcato, S. Bicciato, N. Elvassore, S. Piccolo, Role of YAP/TAZ in mechanotransduction. *Nature* **474**, 179–183 (2011).
43. O. Kim, Y. W. Choi, S. A. Hong, M. Hong, I. H. Chang, H. J. Lee, Fluid shear stress facilitates prostate cancer metastasis through Piezo1-Src-YAP axis. *Life Sci.* **308**, 120936 (2022).
44. L. Niu, B. Cheng, G. Huang, K. Nan, S. Han, H. Ren, N. Liu, Y. Li, G. M. Genin, F. Xu, A positive mechanobiological feedback loop controls bistable switching of cardiac fibroblast phenotype. *Cell Discov.* **8**, 84 (2022).
45. S. Liu, X. Xu, Z. Fang, Y. Ning, B. Deng, X. Pan, Y. He, Z. Yang, K. Huang, J. Li, Piezo1 impairs hepatocellular tumor growth via deregulation of the MAPK-mediated YAP signaling pathway. *Cell Calcium* **95**, 102367 (2021).
46. L. Wang, J. Y. Luo, B. Li, X. Y. Tian, L. J. Chen, Y. Huang, J. Liu, D. Deng, C. W. Lau, S. Wan, D. Ai, K. K. Mak, K. K. Tong, K. M. Kwan, N. Wang, J. J. Chiu, Y. Zhu, Y. Huang, Integrin-YAP/TAZ-JNK cascade mediates atheroprotective effect of unidirectional shear flow. *Nature* **540**, 579–582 (2016).
47. B. Li, J. He, H. Lv, Y. Liu, X. Lv, C. Zhang, Y. Zhu, D. Ai, c-Abl regulates YAPY357 phosphorylation to activate endothelial atherogenic responses to disturbed flow. *J. Clin. Invest.* **129**, 1167–1179 (2019).
48. P. Yuan, Q. Hu, X. He, Y. Long, X. Song, F. Wu, Y. He, X. Zhou, Laminar flow inhibits the Hippo/YAP pathway via autophagy and SIRT1-mediated deacetylation against atherosclerosis. *Cell Death Dis.* **11**, 141 (2020).
49. W. Lee, R. J. Nims, A. Savadipour, Q. Zhang, H. A. Leddy, F. Liu, A. L. Mcnulty, Y. Chen, F. Guilak, W. B. Liedtke, Inflammatory signaling sensitizes Piezo1 mechanotransduction in articular chondrocytes as a pathogenic feed-forward mechanism in osteoarthritis. *Proc. Natl. Acad. Sci. U.S.A.* **118**, e2001611118 (2021).
50. S. Torrino, E. M. Grasset, S. Audebert, I. Belhadj, C. Lacoux, M. Haynes, S. Pisano, S. Abélanet, F. Brau, S. Y. Chan, B. Mari, W. M. Oldham, A. J. Ewald, T. Bertero, Mechano-induced cell metabolism promotes microtubule glutamylation to force metastasis. *Cell Metab.* **33**, 1342–1357.e10 (2021).
51. M. Arra, G. Swarnkar, N. S. Adapala, S. K. Naqvi, L. Cai, M. F. Rai, S. Singamaneni, G. Mbalaviele, R. Brophy, Y. Abu-Amer, Glutamine metabolism modulates chondrocyte inflammatory response. *eLife* **11**, e80725 (2022).
52. C. Lu, C. B. Thompson, Metabolic regulation of epigenetics. *Cell Metab.* **16**, 9–17 (2012).
53. D. A. Chisolm, A. S. Weinmann, Connections between metabolism and epigenetics in programming cellular differentiation. *Annu. Rev. Immunol.* **36**, 221–246 (2018).
54. X. Xia, G. Cao, G. Sun, L. Zhu, Y. Tian, Y. Song, C. Guo, X. Wang, J. Zhong, W. Zhou, P. Li, H. Zhang, J. Hao, Z. Li, L. Deng, Z. Yin, Y. Gao, GLS1-mediated glutaminolysis unbridled by MALT1 protease promotes psoriasis pathogenesis. *J. Clin. Invest.* **130**, 5180–5196 (2020).
55. S. Stegen, G. Rinaldi, S. Loopmans, I. Stockmans, K. Moermans, B. Thienpont, S. M. Fendt, P. Carmeliet, G. Carmeliet, Glutamine metabolism controls chondrocyte identity and function. *Dev. Cell* **53**, 530–544.e8 (2020).
56. A. O. A. P. Iliopoulos, Glutaminase and poly(ADP-ribose) polymerase inhibitors suppress pyrimidine synthesis and VHL-deficient renal cancers. *J. Clin. Investig.* **127**, 1631–1645 (2017).
57. A. Elgogary, Q. Xu, B. Poore, J. Alt, S. C. Zimmermann, L. Zhao, J. Fu, B. Chen, S. Xia, Y. Liu, M. Neisser, C. Nguyen, R. Lee, J. K. Park, J. Reyes, T. Hartung, C. Rojas, R. Rais, T. Tsukamoto, G. L. Semenza, J. Hanes, B. S. Slusher, A. Le, Combination therapy with BPTES nanoparticles and metformin targets the metabolic heterogeneity of pancreatic cancer. *Proc. Natl. Acad. Sci. U.S.A.* **113**, E5328–E5336 (2016).
58. Z. E. Stine, Z. T. Schug, J. M. Salvino, C. V. Dang, Targeting cancer metabolism in the era of precision oncology. *Nat. Rev. Drug Discov.* **21**, 141–162 (2022).
59. R. A. Nishimura, C. M. Otto, R. O. Bonow, B. A. Carabello, J. R. Erwin, R. A. Guyton, P. T. O'Gara, C. E. Ruiz, N. J. Skubas, P. Sorajja, T. R. Sundt, J. D. Thomas, J. L. Anderson, J. L. Halperin, N. M. Albert, B. Bozkurt, R. G. Brindis, M. A. Creager, L. H. Curtis, D. Demets, R. A. Guyton, J. S. Hochman, R. J. Kovacs, E. M. Ohman, S. J. Pressler, F. W. Sellke, W. K. Shen, W. G. Stevenson, C. W. Yancy, 2014 AHA/ACC guideline for the management of patients with valvular heart disease: A report of the American College of cardiology/american heart association task force on practice guidelines. *J. Thorac. Cardiovasc. Surg.* **148**, e1–e132 (2014).
60. T. Wilhelmi, X. Xu, X. Tan, M. S. Hulshoff, S. Maamari, S. Sossalla, M. Zeisberg, E. M. Zeisberg, Serelaxin alleviates cardiac fibrosis through inhibiting endothelial-to-mesenchymal transition via RXFP1. *Theranostics* **10**, 3905–3924 (2020).
61. E. M. Zeisberg, O. Tarnavski, M. Zeisberg, A. L. Dorfman, J. R. Mcmullen, E. Gustafsson, A. Chandraker, X. Yuan, W. T. Pu, A. B. Roberts, E. G. Neilson, M. H. Sayegh, S. Izumo, R. Kalluri, Endothelial-to-mesenchymal transition contributes to cardiac fibrosis. *Nat. Med.* **13**, 952–961 (2007).
62. X. Peng, S. Su, J. Zeng, K. Xie, X. Yang, G. Xian, Z. Xiao, P. Zhu, S. Zheng, D. Xu, Q. Zeng, 4-Octyl itaconate suppresses the osteogenic response in aortic valvular interstitial cells via the Nrf2 pathway and alleviates aortic stenosis in mice with direct wire injury. *Free Radic. Biol. Med.* **188**, 404–418 (2022).
63. M. Yuan, S. B. Breitkopf, X. Yang, J. M. Asara, A positive/negative ion-switching, targeted mass spectrometry-based metabolomics platform for bodily fluids, cells, and fresh and fixed tissue. *Nat. Protoc.* **7**, 872–881 (2012).
64. Q. Zeng, C. Jin, L. Ao, J. J. Cleveland, R. Song, D. Xu, D. A. Fullerton, X. Meng, Cross-talk between the Toll-like receptor 4 and Notch1 pathways augments the inflammatory response in the interstitial cells of stenotic human aortic valves. *Circulation* **126**, S222–S230 (2012).
65. J. Li, Q. Zeng, Z. Xiong, G. Xian, Z. Liu, Q. Zhan, W. Lai, L. Ao, X. Meng, H. Ren, D. Xu, Trimethylamine N-oxide induces osteogenic responses in human aortic valve interstitial cells in vitro and aggravates aortic valve lesions in mice. *Cardiovasc. Res.* **118**, 2018–2030 (2022).

Acknowledgments

Funding: This work was supported by the National Natural Science Foundation of China (82270374 and 82070403 to Q.Z.), the Science and Technology Program of Guangdong Province (2021A0505030031 to Q.Z. and 2017A050501019 to D.X.), the Science and Technology Program of Guangzhou (201707020012 to D.X. and 201804010086 to Q.Z.), the Frontier Research Program of Guangzhou Regenerative Medicine and Health Guangdong Laboratory (2018GZR110105001 to Q.Z.), and the Youth Science and Technology Innovation Talent Program of Guangdong TeZhi plan (2019TQ05Y136 to Q.Z.) **Author contributions:** Conceptualization: G.Z., S.S., and Q.Z. Methodology: G.Z., J.L., H.Z., and D.H. Investigation: G.Z., S.S., Y.L., and J.C. Visualization: L.W., G.X., and X.L. Supervision: S.S., Q.Z., and S.L. Writing—original draft: G.Z. and S.S. Writing—review and editing: G.Z., S.S., D.X., and Q.Z. **Competing interests:** The authors declare that they have no competing interests. **Data and materials availability:** All data needed to evaluate the conclusions in the paper are present in the paper and/or the Supplementary Materials.

Submitted 7 January 2023
Accepted 28 April 2023
Published 2 June 2023
10.1126/sciadv.adg0478